A&A 447, 71–80 (2006)
DOI: 10.1051/0004-6361:20053420

Astronomy & Astrophysics

The luminosity function of X-ray point sources in Centaurus A⋆

R. Voss and M. Gilfanov

Max Planck Institut für Astrophysik, Germany
e-mail: [voss;gilfanov]@mpa-garching.mpg.de

Received 12 May 2005 / Accepted 15 September 2005

ABSTRACT

We have studied the X-ray point source population of Centaurus A (NGC 5128) using data from four archival *CHANDRA* observations. We detected 272 point-like X-ray sources within a radius of 10′ from the centre. Approximately half of these are CXB sources, with the remaining half being LMXBs. The spatial distribution of the LMXBs, both azimuthally averaged and 2D, is consistent with the distribution of the *K*-band light observed in the 2MASS survey. After correction for the incompleteness effect we constrain the LMXB luminosity function down to $\sim 2 \times 10^{36}$ erg s^{-1}, much lower than previous studies of LMXBs in elliptical galaxies. The obtained XLF flattens significantly below $L_X \sim 5 \times 10^{37}$ erg s^{-1} and follows the $dN/dL \propto L^{-1}$ law in agreement with the behaviour found earlier for LMXBs in the Milky Way and in the bulge of M 31.

Key words. galaxies: individual: Centaurus A – X-rays: binaries – X-rays: galaxies

1. Introduction

CHANDRA observations of the bright end, $\log(L_X) \gtrsim 37.5$–38, of X-ray point source populations in nearby elliptical galaxies found a rather steep luminosity distribution with a differential power law index in the ∼1.8–2.5 range (e.g. Colbert et al. 2004; Kim & Fabbiano 2004). This is noticably steeper than X-ray luminosity function (XLF) slopes in spiral and starburst galaxies, ∼1.6 (Grimm et al. 2003). This difference reflects the difference in the composition of the X-ray populations in the early and late type galaxies, dominated by low- and high-mass X-ray binaries, respectively. Extension of the luminosity range available for the study down to $\log(L_X) \sim 36$ revealed a much more complex shape of the XLF of low-mass X-ray binaries (LMXBs). It has been shown to flatten considerably at the faint end and to follow the $dN/dL \propto L^{-1}$ power law below $\log(L_X) \lesssim 37$–37.5 (Gilfanov 2004). Motivated by observational results, Bildsten & Deloye (2004) and Postnov & Kuranov (2005) suggested that the slope of the LMXB XLF in different luminosity regimes is defined by predominantly different sub-types of low-mass X-ray binaries. In the sample of Gilfanov (2004) the faint end of the LMXB XLF was represented by the bulges of two spiral galaxies only – the Milky Way and M 31. On the other hand, the X-ray binaries in elliptical galaxies and spiral bulges could be formed by different mechanisms and have different evolution histories and, consequently, different luminosity distributions. It is therefore important to complement theoretical advances in understanding the XLF of X-ray binaries with firm observational constraints on its behaviour based on a broad range of galactic types, especially at the low luminosity end.

Centaurus A (Cen A) is candidate for such a study. It is massive enough to contain a sufficient number of LMXBs and, on the other hand, is sufficiently nearby to reach luminosities below $\sim 10^{37}$ erg s^{-1} with moderate observing times. It has been widely studied in X-rays, and it has been observed 10 times with *CHANDRA*. These observations have been used to obtain information about the nucleus (Evans et al. 2004), the interstellar medium (Kraft et al. 2003), the jet (Kraft et al. 2002; Hardcastle et al. 2003) the shell structures (Karovska et al. 2002) and the off-centre point source population (Kraft et al. 2001). The objective of the present study is the population of LMXBs in Cen A, namely their spatial and luminosity distribution. Studying the latter, we will focus specifically on the low luminosity domain, $\log(L_X) \sim 36.5$–37.5, whose importance has been emphasized above. Combining 4 observations and accurate incompleteness correction enabled us to investigate sources with luminosity by a factor of ∼5–10 lower than in previous studies.

Cen A has a strongly warped dust disc with evidence for star formation, and optical images show a system of filaments and shells. This is probably due to a recent merger (Schiminovich et al. 1994). It is the nearest active galaxy and is considered to be the prototypical Faranoff-Riley class I radio galaxy. It has a very compact nucleus, most likely an accreting massive black hole, with strongly varying intensity. Emanating from this nucleus are milliarcsecond radio jets and a subrelativistic radio/X-ray jet extend ∼6′ towards NE of the nucleus.

⋆ Appendix is only available in electronic form at
http://www.edpsciences.org

Table 1. The *CHANDRA* observations used in this paper.

Obs-ID	Date	Instrument	Exp. Time	RA	Dec	Data Mode
0316	1999 Dec. 05	ACIS-I	36.18 ks	13 25 27.61	−43 01 08.90	FAINT
0962	2000 May 17	ACIS-I	36.97 ks	13 25 27.61	−43 01 08.90	FAINT
2987	2002 Sep. 03	ACIS-S	45.18 ks	13 25 28.69	−43 00 59.70	FAINT
3965	2003 Sep. 14	ACIS-S	50.17 ks	13 25 28.70	−43 00 59.70	FAINT

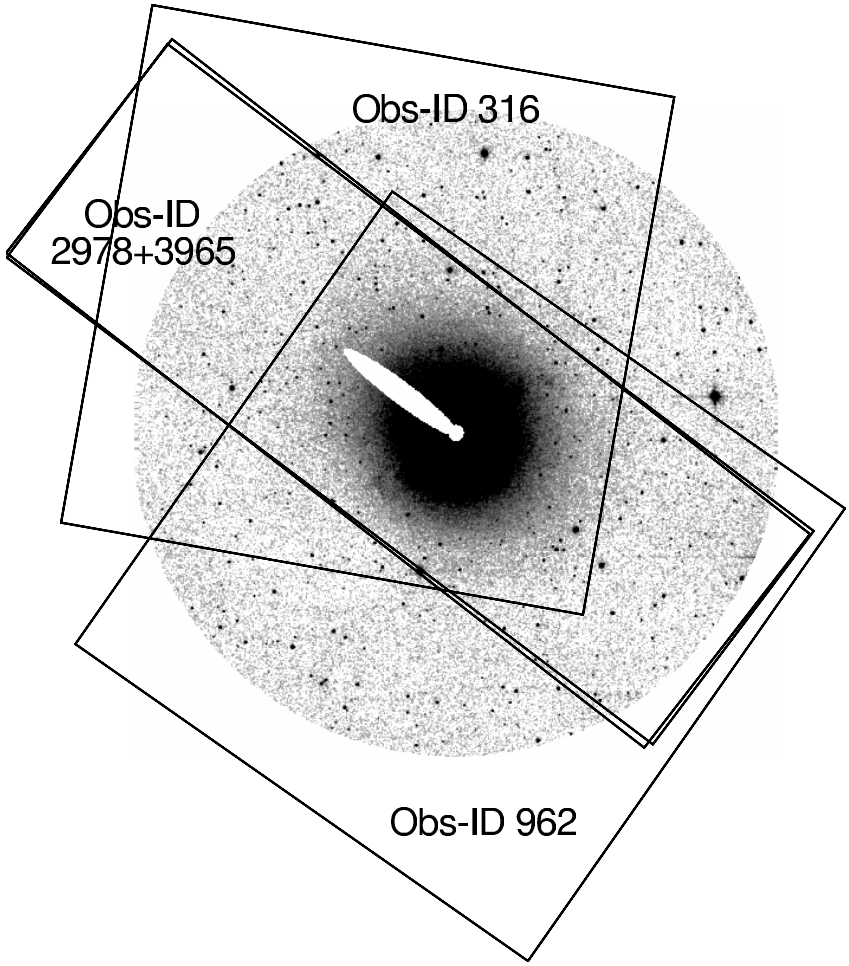

Fig. 1. The 2MASS *K*-band image of the region of Cen A analysed in this paper. The radius of the image is 10′. Also shown are the areas covered by the four *CHANDRA* observations.

Radio lobes extending NE and SW are seen. An exhaustive review of Cen A can be found in Israel (1998).

The paper is structured as follows. In Sect. 2 we describe the data sets and the basic data preparation and analysis. The source list cleaning procedures are presented in Sect. 3, together with source identifications. In this section we also deal with possible periodic variability of the most luminous sources. The properties of the population of X-ray binaries, as well as the background X-ray sources are analysed and compared with previous studies in Sect. 4, including the spatial distribution of the sources and their luminosity function. Section 5 gives the conclusions. We adopt a distance of 3.5 Mpc to Cen A, and that (RA, Dec) = (13 25 27.6, −43 01 08.8) is the centre of the galaxy.

2. Data analysis

The analysis in this paper is based on four *CHANDRA* observations, two of them made with the ACIS-I array (OBS-ID 316 and 962), and the other two with the ACIS-S array (OBS-ID 2978 and 3965). Information about the observations is listed in Table 1; their fields of view overlaid on the *K*-band image of the galaxy are shown in Fig. 1.

Together these four observations cover most of Cen A within a 10′ radius from the centre. The data preparation was done following the standard CIAO[1] threads (CIAO version 3.1; CALDB version 2.28), and limiting the energy range to 0.5−8.0 keV. The ACIS chips sometimes experience flares of

[1] http://cxc.harvard.edu/ciao/

Table 2. The corrections applied to the *CHANDRA* aspect files to align the observations.

Obs-ID	Correction West	Correction North
0316	−0.73 pixel*	−0.42 pixel
0962	+1.58 pixel	+1.44 pixel
2978	−0.53 pixel	−0.18 pixel
3965	−0.31 pixel	−0.85 pixel

* 1 pixel is 0.492″.

enhanced background. For point source detection and luminosity estimation it is not necessary to filter out weak flares, since the increased exposure time outweighs the increased background. We did not find any flares strong enough to filter them out.

We used CIAO wavdetect to detect sources. This program is the most widely used for point source detection in *CHANDRA* data. Some of the parameters we have changed from the default values. Most important are the scales. We have used the $\sqrt{2}$-series from 1.0 to 8.0. This gives a wide enough range of source sizes to account for the variation in point spread function (PSF) from the inner parts of Cen A to the parts 10′ from the centre as well as enough middle scales. We also used maxiter = 10, iterstop = 0.00001 and bkgsigthresh = 0.0001. The effect of changing these parameters is that more iterations are done in the process of removing sources when creating backgound files, at the expense of computing time. Finally we set the parameter eenergy = 0.8 (the encircled fraction of source energy used for source parameter estimation), which gives larger areas for source parameter estimation at the risk of source merging, see Sect. 3.

First we detected sources in the inner region of Cen A covered by all four observations. From these sources we then chose 40 that are bright enough to have the positions determined precisely and that existed in all four observations. We used these sources to determine the average positions of the sources and the offsets for the individual observations. The statistical uncertainties of the source positions are typically 0.3−0.5 pixel. Assuming that the errors are uncorrelated gives an uncertainty of ∼0.05 pixel in the calculated offsets of the observations. Using CIAO dmtcalc we then corrected the aspect and events file for each observation. The corrections applied are listed in Table 2. This step was performed in order to make the observations aligned for combination, not to get better absolute astrometry, which will be dealt with in Sect. 3.

We used CIAO reproject_events to reproject observations 316, 962 and 2978 into the sky coordinates of observation 3965. The files were then merged and the wavdetect task was applied again to the combined image. The output count rate for each detected source is calculated inside a source cell and the local background is subtracted. For each source we extracted the PSF using CIAO psfextract task and calculated the percentage of the counts expected to lie inside each source cell. This was done for each of the four observations, and the result was averaged using the values of the exposure maps as weights. For most sources this percentage is above 97 per cent, and only

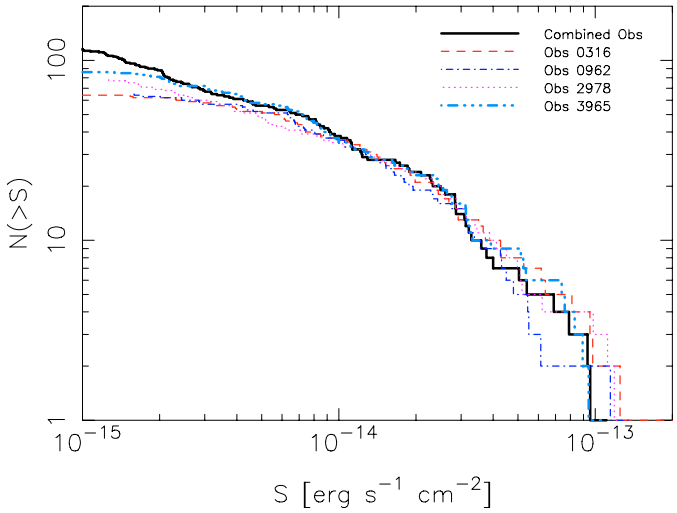

Fig. 2. Comparison of the cumulative $\log(N) - \log(S)$ distribution found in each of the separate observations and in the combined image. Only sources from the inner region, contained in all four observations, have been used and incompleteness correction has not been applied. The incompleteness begins to have effect at a few $\times 10^{-15}$ erg s^{-1} cm^{-2} for the combined image and at $\sim 7-8 \times 10^{-15}$ erg s^{-1} cm^{-2} for the individual observations.

four sources have values lower than 70 per cent. An exposure map was created for each of the observations, assuming the energy distribution to be a powerlaw with photon index of 1.7 and Galactic absorption of 8.4×10^{20} cm^{-2} (Dickey & Lockman 1990). We assumed the same spectrum to convert the observed count rates to unabsorbed source luminosities.

In the very inner parts of Cen A there is strong X-ray emission from hot gas and the central AGN. At the same time there is a large number of point sources within a small area making crowding a serious problem. We have therefore excluded the area within a radius of 30 pixels (∼15″) from the centre of the galaxy.

Simulations using the observed source distribution as input show that excluding this inner region limits crowding to less than 4% of the sources (Sect. A.1). Also the part of the galaxy dominated by the X-ray jet has been excluded. The excluded regions are evident from Fig. 1.

In each of the four observations, readout streaks caused by the bright central region of Cen A are seen. As in different observations they cover different regions of the image, for each streak we have searched for sources and estimated their parameters using a combined image of the observations, excluding the one containing this streak.

To check for differences between the four observations and between the individual observations and the combined observation, we have created the cumulative point source luminosity function for each, taking only sources from the central region, where all four observations overlap, see Fig. 1. The results can be found in Fig. 2. A large fraction of the sources are variable. For these sources, using the luminosities estimated from the combined image is equal to using the average luminosities. We used the Kolmogorov-Smirnov (KS)-test to compare the $\log(N) - \log(S)$ distribution obtained in the individual

observations with that based on the combined data. To minimize incompleteness effects only sources with fluxes higher than 3×10^{-15} erg s^{-1} cm^{-2} were used. The lowest probability found was 68 per cent (for Obs-ID 316). This confirms that the source variability does not modify the flux distribution of the point sources in a galaxy like Cen A at a detectable level.

3. The source list

Several effects can compromise the source list generated from CIAO wavdetect. This includes extended sources and false sources due to background fluctuations. The background due to the diffuse emission is high, especially in the inner parts of Cen A, and many structures can be seen in the image. The "bubble" ∼5′ south-west of the centre is an example (Kraft et al. 2003). Some of these structures might be misinterpreted as point sources. We have visually inspected the images and for each source compared the photon distribution with the distribution expected from the PSF. As a result we rejected 18 sources. As indicated by the shapes, none of the rejected sources is likely to be a supernova remnant. Some of the rejected sources are filamentary structures in the diffuse component and the rest are caused by local variations in the emission of the diffuse component. The characteristic length scale of the latter is $\gtrsim$100 pc. Due to the low luminosity of the rejected sources, it is not possible to classify them according to their spectra.

Another potential problem could be merging of sources. We have used a high value (80 per cent) of the enclosed percentage of PSF in CIAO wavdetect because it gives a good estimation of source parameters. On the other hand, such a high value in some cases leads to two sources being detected as one source. To check for this, we ran CIAO wavdetect again with smaller enclosed percentages of the PSF. We find no sources that are merged because of the high enclosed percentage of the PSF.

After the filtering, the final list of X-ray sources contains 272 objects. It is presented in Table A.1. Kraft et al. (2001) analysed the two ACIS-I observations of Cen A (Table 1) and detected 246 X-ray sources. Of these, 205 sources are located within $r < 10'$ of the center of the galaxy analysed here. 184 of these sources are in our source list, which therefore contains 90 previously undetected sources. The ∼1/3 increase in the total number of detected sources is due to a factor of $\gtrsim$2−4 increase in the exposure time of the main body of the galaxy (Fig. 1, Table 1).

3.1. Background and foreground sources

A fraction of the detected sources are foreground or background objects. Some (but not all) of them can be identified using either their X-ray spectra, or from observations at other wavelengths. Since this paper concerns the statistical properties of the X-ray point source population, we have adopted the following strategy. We exclude foreground sources as much as possible (6 such sources are excluded, see Sect. 3.2), but do not attempt to remove background sources, which are by far the most significantly contaminating factor (about half of the detected sources are background sources, see Sect. 4.3). Their contribution to the surface brightness and luminosity distributions is instead taken into account in the statistical sense, based on the results of the cosmic X-ray background (CXB) source counts.

3.2. Optical identifications

We check the absolute astrometry using USNO-B1.0 (Monet et al. 2003) and GSC 2.2 (Morrison et al. 2001) catalogues. We find that for a search radius of 2.0″ the rms deviation of the positions is 1.1″. This is comparable to the quoted positional uncertainties of the optical catalogues as well as that of the Chandra X-ray source list, confirming reasonable astrometric accuracy of the latter. Adding a systematic shift of 0.5″ in any direction results in larger rms deviations. The number of matches is significantly higher than the expected number of chance coincidences. For the search radius of 2.0″ the expectation value is ∼8 with 37 matches found for USNO-B1.0 and ∼3 with 18 matches found for GSC 2.2.

For the actual identification of Chandra sources we used the results of the dedicated optical studies of the Cen A region by Peng et al. (2004), Minniti et al. (2003) and Woodley et al. (2005). Although the former three surveys were aimed specifically at globular cluster population of Cen A they also have identified a number of foreground stars, H_α emittors and several AGNs. We also used results of Graham & Fasset (2002). In total we identified 6 X-ray sources as foreground stars, leaving 266 sources of presumably extragalactic origin – either intrinsic Cen A sources or background AGNs. Of these, 37 were identified with the globular clusters in Cen A. The results of this work are presented in column 8 of Table A.1.

About ∼2/3 of the USNO and GSC matches were found to be globular clusters or likely globular clusters in Peng et al. (2004) and Minniti et al. (2003). The remaining 12 out of 37 sources do not appear in these papers. This is close to but slightly higher than the number of 8 random matches expected for the value of the search radius used in the analysis. Some of these sources also might be background AGNs or undetected globular clusters. Therefore we kept them all in the sample. We note that excluding them from the following analysis does not change our results in any significant way.

3.3. Hα-sources

Eight sources within 4′ from the centre of Cen A coincide with Hα-emitting regions found in Minniti et al. (2003). All of them are located in the dust lanes region, have X-ray luminosities in the 10^{36}–5×10^{37} erg s^{-1} range and can potentially be associated with high-mass X-ray binaries. The optical magnitudes of the Hα sources indicate that they may be young star clusters as well as individual X-ray binaries. In order to search for further indications of the high-mass X-ray binary (HMXB) nature of these sources we have compared their spectral properties with other sources and searched for periodic variability in their X-ray emission. As discussed in more detail below, no coherent pulsations were detected from any of the bright X-ray sources, although the upper limits are at a rather moderate level of ∼25 per cent pulsed fraction.

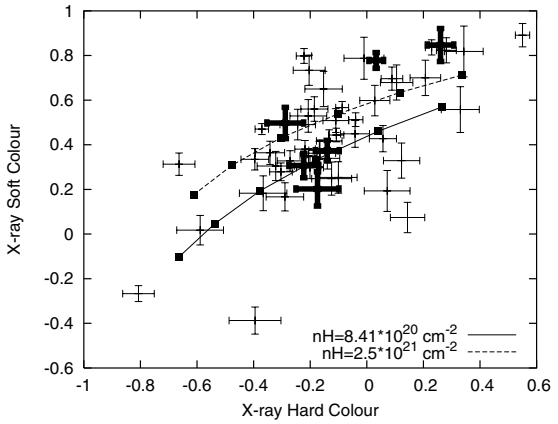

Fig. 3. The color–color diagram of the brightest, >200 counts, sources within 5 armin from the centre of Cen A. The sources coinciding with H_α-emitting regions are shown in bold. For reference, the two lines show the hardness ratios of power law spectra for two different values of absorption. The filled squares are at photon indices of 0.5, 1.0, 1.5, 2.0, 2.5, 3.0 from right to left. The hard and soft colours are defined as $HC = (H - M)/(H + M)$, $SC = (M - S)/(M + S)$, where S, M and H are the number of photons detected in the 0.5−1.0 keV, 1.0−2.0 keV and 2.0−8.0 keV energy range respectively.

The accreting X-ray pulsars, constituting the vast majority of the neutron star HMXBs, are known to have notably harder spectra in the ∼1−20 keV energy range than LMXBs and often show significant intrinsic absorption. Therefore comparison of the spectral properties of the Hα objects with other X-ray sources (which in the central part of Cen A are mostly LMXBs, Sect. 4) can help to clarify the nature of the former. However, the X-ray colour-colour diagram of the sources within 5′ from the centre of Cen A, shown in Fig. 3, does not reveal systematic differences between Hα and other sources, nor have we found any systematic differences from the direct spectral fits of the brightest sources.

Comparing Fig. 3 with Fig. 4 of Prestwich et al. (2003) and noting the slight difference in energy bands, it can be seen that the main part of our sources is located in the region corresponding to LMXBs. There is a small population of harder sources, of which two are Hα objects and also a few softer sources. From their position in the diagram, they could be HMXBs and thermal supernova remnants, respectively. Such identifications are not possible with to the colours alone for two reasons. One is that the absorption inside Cen A varies strongly with position, which has the effect of enhancing the scatter of LMXBs in the diagram. The second reason is that there is a contribution of CXB sources. This population is known to consist of two subpopulations, a hard and a soft one. These populations would be expected to coincide with the HMXBs and the supernova remnants, respectively, in the diagram.

As our results were not conclusive enough, we decided to keep the Hα sources in the sample, bearing in mind that their nature still needs to be clarified. Due to their relatively small number they do not significantly affect the following analysis of the spatial and luminosity distributions.

3.4. Globular cluster sources

37 X-ray sources coincide with known globular clusters. Interpreting this number, one should take into account that only ∼20−25 per cent of the expected number of globular clusters in Cen A have been identified (Woodley et al. 2005). The identified sample is strongly biased, both with respect to the spatial distribution of the clusters and their luminosity distribution. Furthermore, the detection of the globular clusters is not independent of the X-ray observations, as X-ray source catalogues have been used to search for globular clusters (e.g. Minniti et al. 2003). It is therefore not possible to perform a rigorous comparison of the luminosity function and spatial distribution of the globular cluster X-ray sources with the sources residing outside globular clusters. Considering the sources brighter than 3×10^{37} erg s^{-1} (i.e. unaffected by incompleteness effects) there are 15 known globular cluster X-ray sources, whereas the number of sources outside globular clusters is 40. If the expected number of 22 CXB sources (see Sect. 4.3) is subtracted, we find 18 "field" LMXBs outside (or in undetected) globular clusters. Above this luminosity the XLF of globular cluster sources is similar to that of the field LMXBs. Below this luminosity the field LMXB XLF is much steeper than that of globular cluster sources. This can easily be caused by incompleteness effects, which cannot be corrected for without knowledge of the spatial distribution of the globular cluster sources (see Appendix). We also note that in the outer region there are 7 globular cluster sources, with $L_X \geq 10^{37}$ erg s^{-1} whereas we expect ∼9 LMXBs in total (see Sect. 4.1.1).

3.5. Search for coherent pulsations

We searched for periodic variability in the light curves of the sources with more than 400 detected source counts and more luminous than 6.0×10^{37} erg s^{-1} (24 sources in total). Each *CHANDRA* observation was tested separately. Events were extracted from the 4 sigma source ellipses in `wrecon` and the light curves with ≈3.2 s time resolution were produced. The power spectra were calculated using the STARLINK[2] task `period`. Pulsations were searched for in the range of trial periods from $P \approx 6.4$ s, defined by the Nyquist frequency of the Chandra time series, to $P = 2000$ s. Except 3 sources showing variability due to the telescope dithering carrying them over the detector edge, in only one did the power exceeded the level corresponding to 99 per cent confidence. The period of 55.8 s was found for the source #135 (Table A.1) in Obs. 2978 and had a significance of 99.4 per cent. This significance takes into account the number of trial periods in one power spectrum but not the number of power spectra analyzed (74). In the other 3 observations of the source the power density spectrum did not show any signs of pulsations at this period. Given the total number of power spectra investigated it is likely that this detection is a result of a statistical fluctuation. Even for the most luminous sources, pulsed fractions of ∼25 per cent would be needed for detection at the 99 per cent confidence level.

[2] `http://www.starlink.ac.uk`

Table 3. Expected and observed numbers of point sources (Sect. 4.1).

L_X	Predicted				Obs.
erg s^{-1}	LMXB	HMXB	CXB[(1)]	Total[(1)]	Total[(2)]
$>10^{37}$	81	10	34 (47)	125 (138)	136
$>2\times10^{36}$	155	27	98 (135)	280 (317)	321

[(1)] – the CXB numbers are based on the soft (hard) band counts from Moretti et al. (2003), see Sect. 4.1.3; [(2)] – after the incompleteness correction.

4. Populations of X-ray sources in the field of Centaurus A

In the central $r < 10'$ of Cen A (excluding the nucleus and the jet, Fig. 1, Sect. 2) we detected 136 sources with $L_X > 10^{37}$ erg s^{-1} and 252 (≈321 after the incompleteness correction) sources with $L_X > 2\times10^{36}$ erg s^{-1} (Tables A.1, 3).

4.1. Expected numbers

4.1.1. Low mass X-ray binaries

LMXBs are related to the population of old stars, and there is therefore a correlation between their number and the stellar mass of a galaxy (Gilfanov 2004). In order to estimate the expected number and luminosity distribuition of LMXBs we used a K-band image from the 2MASS Large Galaxy Atlas (Jarret et al. 2003) and integrated the flux emitted in the parts of Cen A analysed in this paper. This gives the K-band luminosity of $L_K = 8.6\times10^{10}\ L_\odot$. To convert it to the stellar mass we use the color-dependent K-band mass-to-light ratio from Bell & De Jong (2001). For the extinction corrected optical color of Cen A, $(B-V)\approx0.88$, the mass-to-light ratio is $M_*/L_K\approx0.76$. This gives the stellar mass of $5.5\times10^{10}\ M_\odot$, assuming that the absolute K-band magnitude of the sun is equal to $M_{K,\odot}=3.39$. Using the results of Gilfanov (2004) we predict ≈81 LMXBs with $L_X > 10^{37}$ erg s^{-1}, and ≈155 with $L_X > 2\times10^{36}$ erg s^{-1}.

4.1.2. High mass X-ray binaries

Being young objects, HMXBs are associated with star formation and, as expected for an elliptical galaxy, are by far a less significant contribution to the population of X-ray binaries than LMXBs. In terms of absolute rates, star formation in Cen A is mostly associated with the dust disk. From their analysis of IRAS data, Marston & Dickens (1988) found the total far infra-red (FIR) luminosity of the Cen A disc to be $9.7\times10^9\ L_\odot$ ($L_\odot = 3.8\times10^{33}$ erg s^{-1}). From this luminosity we subtracted the emission from the central region which is mostly due to the active nucleus, $1.5\times10^9\ L_\odot$, and corrected the distance from the 5 Mpc assumed in Marston & Dickens (1988) to the 3.5 Mpc adopted in this paper. This gives $L_{\rm FIR}\approx4.0\times10^9\ L_\odot$. Assuming that the total infrared luminosity is $L_{\rm TIR}\approx2L_{\rm FIR}$ and using the SFR calibration of Kennicutt (1998) we find $SFR\approx1.4\ M_\odot$ yr^{-1}. We used the calibration of Grimm et al. (2003) to calculate the expected number of HMXBs (see comment in Shtykovskiy & Gilfanov 2005 regarding the normalization).

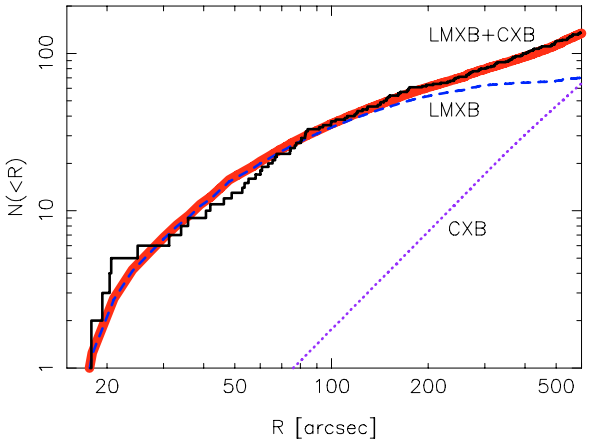

Fig. 4. The radial distribution of observed sources (solid line), compared to the best fit model (thick grey line) and the contributions of LMXBs and CXBs.

From this we get the expectation of ≈10 HMXBs brighter than 10^{37} erg s^{-1}, and ≈27 sources brighter than 2×10^{36} erg s^{-1}.

4.1.3. Background X-ray sources

To estimate the number of background sources we use the results of the CXB $\log(N) - \log(S)$ determination by Moretti et al. (2003). We use the source counts in the soft and hard bands (their Eq. (2)) and convert the fluxes to the 0.5−8.0 keV band, assuming a powerlaw spectrum with a photon index of 1.4. For the total area of our survey of 0.079 deg^2 we obtain from the source counts in the soft band ≈34 CXB sources above the flux corresponding to 10^{37} erg s^{-1}, and ≈98 above 10^{36} erg s^{-1}. From the hard band counts the predicted numbers are ≈47 and ≈135 sources. The predictions based on the soft and hard $\log(N) - \log(S)$ differ because of the well recognized fact that source counts in different energy bands and flux regimes are dominated by different types of sources. This is further discussed in Sect. 4.3. Furthermore the normalization of the CXB source counts is subject to uncertainy due to the cosmic variance. Its rms amplitude is ∼20−25% (see e.g. Cappelluti et al. 2005).

The results of the above calculations are summarized in Table 3. For the total number of point sources, the agreement between observed and predicted values is surprisingly good, given the amplitude of uncertainties involved. In the following two subsections we derive from the data, and compare with the predictions, the abundances of individual types of X-ray sources. This is done in two independent ways – based on the radial distribution of the sources (Sect. 4.2) and on their flux/luminosity distribution (Sect. 4.3).

4.2. Spatial distribution of point sources

We begin with the azimuthally averaged radial profile (Fig. 4). As it follows from the results of the previous section the two major contributiors to the population of point sources in the field of Cen A are low-mass X-ray binaries (∼1/2−2/3 of the sources, depending on the luminosity) and background AGNs

(∼1/3−1/2). Correspondingly, we model the observed distributions as a superposition of two functions, describing their respective contributions. The spatial distribution of the LMXBs has been shown (Gilfanov 2004) to follow, to first approximation, the distribution of the stellar mass. The latter can be represented by the distribution of the K-band light and was computed using the K-band image of Cen A from the 2MASS Large Galaxy Atlas (Jarret et al. 2003). The density of the CXB sources can be assumed to be flat on the angular scales under consideration, therefore the CXB growth curve is proportional to the enclosed solid angle. In computing both radial profiles we took into account that some areas were excluded from the analysis (Fig. 1). The only free parameter of the model is the ratio of normalizations of the LMXB and CXB distributions. The (unknown) distribution of HMXBs has not been included as it is unlikely to exceed 10% of the total number of sources (Sect. 4.1.2).

The model has been compared with the observed distribution of sources more luminous than 10^{37}erg s^{-1}. This value of the luminosity threshold was chosen in order to include as many sources as possible and, on the other hand, to keep incompleteness effects insignificant. The model adequately describes the data (Fig. 4) as confirmed with the KS-test, with a probability of 96 per cent. The best fit LMXB fraction, determined from the Maximum Likelihood (M-L) fit to the the unbinned radial distribution data, is 51.7 ± 5.9 per cent, corresponding to 70.3 ± 10.0 LMXBs and 65.7 ± 9.8 CXB sources. Compared to Table 3, the abundance of LMXBs is surprisingly close to the expectated value. The number of CXB sources, on the other hand, is higher than the expectation. This will be further discussed in Sect. 4.3.

The same LMXB+CXB model was also compared with the radially averaged azimuthal and two-dimensional distributions. The KS test of the unbinned two-dimensional distribution of the point sources (e.g. Press et al. 1992) gave a probability of 24%. The azimuthal distribution of the sources within 5′ (to exclude the outer regions dominated by CXB) has the KS-probability of 10−20 per cent depending on the starting point. Also we checked whether there was any azimuthal dependence on the radial profiles, by dividing the observations into two and three slices and comparing them using the KS-test. Trying a lot of different angles, we found no evidence for such a dependence. Due to the low number of sources, such evidence would not be found unless the effect was strong.

This analysis confirms that within the statistical accuracy of the data, the spatial distribution of the LMXBs is consistent with that of the K-band light. This implies, in particular, that no additional component corresponding to HMXBs is required by the data. However, this result is not very constraining, given the rather small expected number of HMXBs, ≈10.

4.2.1. Sensitivity of the spatial distribution analysis

In order to probe the sensitivity of the above analysis we performed the following test. The LMXB distribution was streched with respect to the center of the galaxy by some scale factor, the new best fit value of the CXB to LMXB ratio was found using same method as before, and the consistency of new best fit model with the data was checked with the KS test. Then the range of values or the scale factor was found beyond which the KS probability decreased below 5 per cent indicating deteriorated quality of the approximation. The following ranges for the scale factor values were obtained: $0.4 \lesssim \eta \lesssim 1.9$ for the radial profile analysis and $0.2 \lesssim \eta \lesssim 2$ for the 2-dimensional image.

These numbers indicate a rather moderate sensitivity of the spatial distribution analysis. Sensitivity limitations of this kind are unavoidable when analysing individual galaxies. Further exposure of the inner 10′ of the galaxy can improve the luminosity limit below which incompleteness effects have to be taken into account. Observations with the telescope pointing to the outskirts of the galaxy could be useful too, as they could help to constrain the local CXB normalization. Also a very careful study of the source distribution at luminosities where incompleteness is a problem could increase the sensitivity. Another approach is to study combined source density distributions for several (many) galaxies.

4.3. Source counts and the cosmic X-ray background source density

We divided Cen A into three annuli according to the ratio of predicted numbers of LMXBs and CXB sources: $r < 2.5'$, $r = 2.5-5'$, $r = 5-10'$). The inner and outer regions are expected to be dominated by LMXBs and CXB sources respectively, while the middle one contains comparable numbers of sources of both types (e.g. Fig. 4). In analysing the luminosity functions and $\log(N) - \log(S)$ distributions we used the procedure described in Appendix A to correct for incompleteness effects.

We estimate the normalization of the CXB $\log(N) - \log(S)$ distribution from the source counts in the outer region. This region is far enough from the inner parts of the Cen A to keep the number of sources related to the galaxy low, while close enough to the aimpoints of the observations to have a reasonable sensitivity. In this region the incompleteness corrected number of sources with the 0.5−8 keV flux exceeding 2.7×10^{-15} erg s^{-1} cm^{-2} (luminosity 4.0×10^{36} erg s^{-1}) is 101.3 from which 13.4 are expected to be LMXBs. The implied number of CXB sources is ≈88, which we compare with the results of the radial profile analysis from the previous section and with results of dedicated CXB source counts. For this comparison we express the CXB normalization in units of the number of sources per deg^2 with 0.5−8.0 keV flux $S_X > 6.8 \times 10^{-15}$ erg s^{-1} cm^{-2}. The results of the CXB surveys are transformed to the 0.5−8.0 keV energy range assuming a power law spectrum with the photon index of 1.4. We used the source counts in both their soft (0.5−2.0 keV) and hard (2.0−8.0 keV) bands. The results are shown in the two columns in the upper part of Table 4. The last two lines in Table 4 present the results of the radial profile analysis and of the source counts in the $r = 5'-10'$ ring. Note that although these two numbers are not statistically independent, they are obtained from different considerations. The radial profile analysis is based on

Table 4. CXB normalization found in various surveys and in this paper.

Survey	soft band	hard band
CDF-S	332 ± 70	686 ± 71
CDF-N	437 ± 80	791 ± 73
Cappelluti et al. (2004)	350 ± 28	419 ± 43
Cowie et al. (2002)	–	456 ± 30
Moretti et al. (2003)	422	579
Obs–ID 1671 (CDF-N)	519 ± 71	
Radial profile (Cen A)	832 ± 124	
$5' < r < 10'$ counts (Cen A)	804 ± 86	

The normalization is expressed as the number of sources per deg^2 with 0.5−8.0 keV flux $S_X > 6.8 \times 10^{-15}$ erg s^{-1} cm^{-2}. The two columns give the numbers computed from the soft and hard band counts respectively. The for CDF-fields data listed in the upper part of the table are from Rosati et al. (2002), in the lower part – from this paper.

sources with $L_X \geq 10^{37}$ erg s^{-1} in the entire $r \leq 10'$ region and relies heavily on the assumption about the spatial distribution of the LMXB component. The source counts in the outer region use all sources in the $5' \leq r \leq 10'$ with a luminosity above 10^{36} erg s^{-1} and are significantly less dependent on the assumption of the LMXB spatial distribution.

As it has been already mentioned, there is a significant difference between the normalizations found from the hard and soft bands. This is related to the fact that different types of sources give dominant contributions to the hard and soft bands. Theoretically, the two bands can be reconciled using different spectral shapes for the the flux conversion, but this would introduce additional uncertainties and an investigation of this kind is beyond the scope of this paper. In addition, there is also a considerable spread in the CXB normalizations in the same energy band obtained in different surveys. This spread is partly due to the cosmic variance and partly it is likely to be caused by the difference in the analysis procedures and relative calibrations of different instruments.

In order to do a direct comparison with the empty fields source counts in the 0.5−8.0 keV energy band, we have analysed one observation from the CDF-N (Obs-ID 1671), using the same data analysis procedure as we used for Cen A. The column density of neutral hydrogen was set to 1.5×10^{20} cm^{-2} (Dickey & Lockman 1990). To avoid incompleteness effects, we only used sources observed in regions with exposure above 4.4×10^7 s cm^2. This limits the field to 0.058 deg^2. Above a flux of 2.7×10^{-15} erg s^{-1} cm^{-2} (equal to the flux used to extimate the CXB normalization in the outer region of Cen A) we find 53 sources. This number can be directly compared with 88 CXB sources detected in the outer annulus in the Cen A field (by chance the two areas coincide). In order to facilitate comparison with the other CXB surveys, we transform this number to the units of Table 4, using the $\log(N) - \log(S)$ from the soft band of Moretti et al. (2003).

Even with the spread in values found from the various surveys, the CXB normalization in the Cen A field appears to be higher than the typical numbers obtained in the dedicated CXB studies, with the exception of the hard band counts of the Chandra Deep Fields, according to the analysis of Rosati et al. (2002). The latter two excluded, the density of CXB sources appears to be enhanced by a factor of ∼1.4−2. Although this is larger than the rms variation between different fields typically quoted in the literature, ∼20−25 per cent, the observed number is not exceptionally high and still lies within the spread of the CXB density values (e.g. Cappelluti et al. 2005).

4.4. LMXB X-ray luminosity function

The luminosity function of LMXBs determined from the two inner regions is shown in Fig. 6. In subtracting the contribution of CXB sources we used the $\log(N) - \log(S)$ distribution from Moretti et al. (2003) with the normalization determined in the Sect. 4.3. While the CXB contribution is unimportant in the innermost region $r \leq 2\farcm5$, it accounts for about half of the sources in the middle region $2\farcm5 \leq r \leq 5'$. As is obvious from Fig. 6, both distributions are consistent with each other and with the average LMXB XLF in the local galaxies determined by Gilfanov (2004), with the possible exception of the the lowest luminosity bin of the middle region, which deviates by $\sim 1.5\sigma$.

To further constrain the parameters of LMXB XLF in Cen A we fit the luminosity distribution in the inner region with a power law with two breaks, identical to the one used in Gilfanov (2004). Since there are no sources luminous enough to constrain the upper break and the slope beyond that, we have fixed them at the average values: $L_{b2} = 5.0 \times 10^{38}$ erg s^{-1}, $\alpha_3 = 4.8$. The best fit values of other parameters are: the low luminosity slope $\alpha_1 = 1.02^{+0.12}_{-0.13}$, a break at $L_{b1} = 5.0^{+1.0}_{-0.7} \times 10^{37}$ erg s^{-1} and a slope after the break $\alpha_2 = 2.6 \pm 0.4$. The slopes refer to the differential distribution, the parameter errors are 1σ statistical errors only. Notice that the break value found for differential XLFs is systematically higher than the break value found for cumulative XLFs, using the same data, see e.g. Kaaret (2002). These parameters are insensitive to whether the CXB component is accounted for or not.

A large uniformly analysed sample of the XLF of LMXBs in elliptical galaxies was presented by Kim & Fabbiano (2004). They find an average differential slope of 1.8 ± 0.2 in the luminosity range L_X = a few $\times 10^{37}$ to 5×10^{38} erg s^{-1}. This is consistent with our results from the inner region. A KS-test gives 73 per cent probability that the observed luminosity distribution above $L_X = 1.0 \times 10^{37}$ erg s^{-1} could be produced by their LMXB XLF. On the other hand it is clear that at the faint end of the XLF the extrapolation of their results is inconsistent with our observations. For sources more luminous than $L_X = 5.0 \times 10^{36}$ erg s^{-1}, a similar KS-test gives 3.4 per cent, and for lower luminosities the probability decreases further.

The LMXB XLF based on the combined data of $r \leq 5'$ is plotted in Fig. 7 along with luminosity distributions of LMXBs in the Milky Way and M 31. This plot further illustrates the qualitative and quantitative similarity of the LMXB luminosity distributions in Cen A and bulges of spiral galaxies. This is the first study to extend the LMXB XLF in elliptical galaxies below $\sim$few$\times 10^{37}$ erg s^{-1}. Spiral and elliptical galaxies have different

evolutionary histories and it could differ in the properties of their LMXB populations. As demonstrated here, the luminosity functions nevertheless seem very similar, except for the break luminosity which could be somewhat higher in Cen A than in the Milky Way and M 31. Whether this reflects a systematic difference between LMXBs in galaxies of different type is yet to be investigated.

4.5. X/M_* ratios

In the inner (middle) region there are 53 (27) sources with $L_X > 10^{37}$ erg s^{-1}, with an integrated luminosity of $L_X = 2.3 \times 10^{39}$ (1.3×10^{39}) erg s^{-1}. We expect the CXB contribution to be $N_{CXB} = 3.8$ (13.4), corresponding to a luminosity of 1.9×10^{38} (6.7×10^{38}) erg s^{-1}. From the K-band light we estimate that the stellar mass is 3.6×10^{10} (1.3×10^{10}) $M_\odot$, and this gives us the ratios $N_X/M_* = 13.7 \pm 1.9$ (10.5 ± 2.0) sources per 10^{10} $M_\odot$ and $L_X/M_* = 6.4$ (4.8) $\times 10^{38}$ erg s^{-1} per 10^{10} $M_\odot$. The values for the two regions are consistent. They are also in a good agreement with the values for different nearby galaxies listed in Table 2 of Gilfanov (2004) as well as with the average values of $\langle N_X/M_* \rangle = 14.3$ and $\langle L_X/M_* \rangle = 8.0 \times 10^{38}$ erg/s per 10^{10} $M_\odot$.

The X/M_* ratios obtained in this paper are by a factor of 2 lower than the values for Cen A in Gilfanov (2004). He reported problems in approximating the multi-aperture K-band photometry data for Cen A galaxy. Indeed, we recomputed the K-band luminosity for the same region using the 2MASS K-band image and obtained ≈2 times larger number. This explains the lower values of N_X/M_* and L_X/M_* found in this paper. As these numbers are derived from the real K-band images rather than from extrapolation of the multi-aperture K-band photometry, they better represent the true values of the X/M_* ratios.

5. Summary and conclusions

We have used archival data of *CHANDRA* observations to study statistical properties of the point source population of Cen A. Our primary goal was to investigate the faint end of the LMXB luminosity distribution in an elliptical galaxy and to compare it with LMXB XLF in bulges of spiral galaxies.

To achieve this we assembled as deep a survey of the central part of the galaxy as permitted by the available data and implemented an adequate correction for the incompleteness effects.

Cen A is the closest giant elliptical galaxy and the only one with enough exposure time by *CHANDRA* to perform such a study. As Cen A is a merger remnant, the stellar and LMXB population might differ from those of less disturbed giant ellipticals. It is therefore important to further perform deep studies of the X-ray source population of more normal early-type galaxies.

Using a combined image of four ACIS observations (Table 1, Fig. 1) with the total exposure time of 170 ks we have detected 272 point-like sources within 10′ of the nucleus of Cen A. The luminosity of the weakest detected source is ≈9×10^{35} erg s^{-1} (assuming a distance of 3.5 Mpc), while

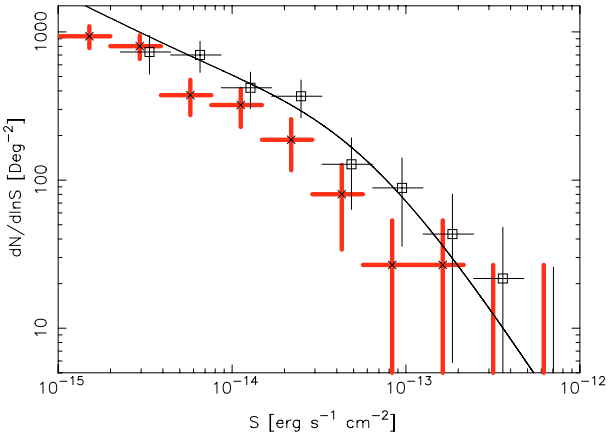

Fig. 5. The source counts (open squares) in the outer region ($5' < r < 10'$). The predicted contribution of LMXBs is subtracted. The thick solid line shows the CXB $\log(N) - \log(S)$ from Moretti et al. (2003). with best fit normalization from this paper. For comparison the source counts in the CDF-N Obs-ID 1671 are shown (crosses).

the source sample starts to be affected by the incompleteness effects below ∼10^{37} erg s^{-1} (Fig. A.1). After correction for incompleteness, the total number of sources with $L_X \geq 2 \times 10^{36}$ erg s^{-1} is ≈321. This number is in good agreement with the prediction based on the stellar mass, the star formation rate in Cen A and the density of CXB sources (Table 3). About half of the detected sources are expected to be X-ray binaries in Cen A, mostly LMXBs; the vast majority of the remaining sources are background galaxies constituting the resolved part of the CXB.

The spatial distribution of the detected sources can be well described by a sum of two components. Of these, one has a density proportional to the K-band light (Fig. 4) and the other is uniform accross the Cen A field. We interpret this as that the former represents low-mass X-ray binaries in Cen A while the latter accounts for the resolved part of the CXB. The normalization of the LMXB component agrees well with the average value derived for the local galaxies by Gilfanov (2004). The normalization of the uniform component and source counts in the exteriors of the galaxy appear to indicate an overabundance of the CXB sources in the direction of Cen A by a factor of ∼1.5 or, possibly, more (Table 4, Fig. 5).

After applying the incompleteness correction and subtracting the contribution of CXB sources we were able to recover the the LMXB luminosity function in the inner $r \leq 5'$ down to $L_X \sim 2 \times 10^{36}$ erg s^{-1} (Figs. 6, 7). This is by a factor of ∼5−10 better than achieved previously for any elliptical galaxy (Kraft et al. 2001; Kim & Fabbiano 2004). The shape of the luminosity distribution is consistent with the average LMXB XLF in nearby galaxies derived by Gilfanov (2004) and for the bright end by Kim & Fabbiano (2004). In particular, we demonstrate that the LMXB XLF in Cen A flattens at the faint end and is inconsistent with extrapolation of the steep power law with differential slope of ≈1.8−1.9 observed above $\log(L_X) \sim 37.5$−38 in the previous studies of elliptical galaxies. Rather, the LMXB XLF in Cen A has a break at $L_X \approx (5 \pm 1) \times 10^{37}$ erg s^{-1} below which it follows the $dN/dL \propto L^{-1\pm0.1}$ law, similar to the behaviour found in the bulges of spiral galaxies.

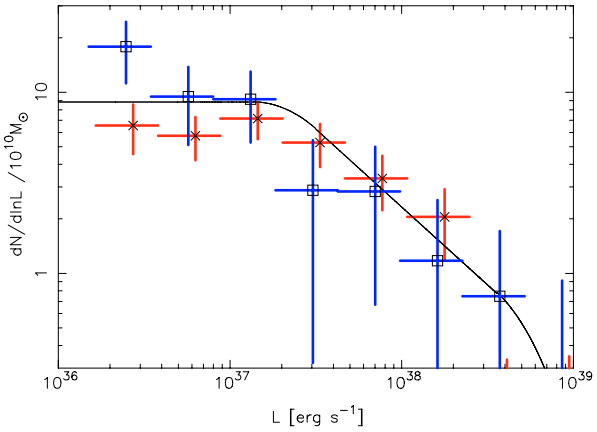

Fig. 6. The differential luminosity functions of LMXBs in the innermost (stars) and middle (squares) annuli, normalized to 10^{10} $M_\odot$ of stellar mass. The CXB contribution is subtracted using the results of Sect. 4.3. The solid line shows the average LMXB XLF from Gilfanov (2004) smoothed with the boxcar filter with the logarithmically constant width equal to the bin width in the observed XLFs.

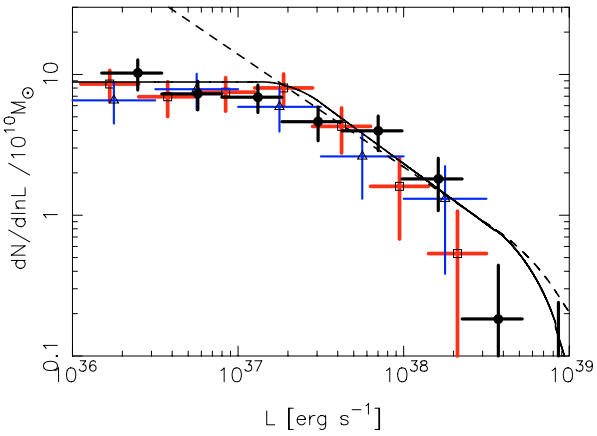

Fig. 7. The luminosity function of LMXBs in the inner $r \leq 5'$ of Cen A (the CXB contribution subtracted) in comparison with LMXB XLFs in the Milky Way (triangles) and M 31 (squares) (from Gilfanov 2004). The latter two are multiplied by constant factors of 1.7 and 0.6 respectively. The solid line shows the average LMXB XLF in the nearby galaxies as determined by Gilfanov (2004), the same as in Fig. 6. The dashed line shows the average LMXB XLF from Kim & Fabbiano (2004) and its extrapolation towards low luminosities. Its normalization was chosen to approximately match our observations.

Acknowledgements. This reaserch has made use of *CHANDRA* archival data provided by the *CHANDRA* X-ray Center and data from the 2MASS Large Galaxy Atlas provided by NASA/IPAC infrared science archive. We would like to thank the referee for useful comments.

References

Bell, E., & De Jong, R. 2001, ApJ, 550, 212
Bildsten, L., & Deloye, C. J. 2004, ApJ, 607, L119
Cappelluti, N., Cappi, M., Dadina, M., et al. 2005, A&A, 430, 39
Colbert, E. J. M., Heckman, T. M., Ptak, A. F., Strickland, D. K., & Weaver, K. A. 2004, ApJ, 602, 231
Cowie, L. L., Garmire, G. P., Bautz, M. W., et al. 2002, ApJ, 566, L5
Dickey, J. M., & Lockman, F. J. 1990, ARA&A, 28, 215
Evans, D. A., Kraft, R. P., Worrall, D. M., et al. 2004, ApJ, 612, 786
Freeman, P. E., Kashyap, V., Rosner, R., & Lamb, D. Q. 2002, ApJS, 138, 185
Gilfanov, M. 2004, MNRAS, 349, 146
Graham, J. A., & Fasset, C. I. 2003, ApJ, 575, 712
Grimm, H.-J., Gilfanov, M. R., & Sunyaev, R. A. 2003, MNRAS, 339, 793
Hardcastle, M. J., Worrall, D. M., Kraft, R. P., et al. 2003, ApJ, 593, 169
Israel, F. P. 1998, A&AR, 8, 237
Jarret, T. H., Chester, T., Cutri, R., Schneider, S., & Huchra, J. P. 2003, AJ, 125, 525
Kaaret, P. 2002, ApJ, 578, 114
Karovska, M., Fabbiano, G., Nicastro, F., et al. 2002, ApJ, 577, 114
Kennicutt, R. C. 1998, ARA&A, 36, 189
Kim, D.-W., & Fabbiano, G. 2003, ApJ, 586, 826
Kim, D.-W., & Fabbiano, G. 2004, ApJ, 611, 846
Kraft, R. P., Kregenow, J. M., Forman, W. R., Jones, C., & Murray, S. S. 2001, ApJ, 560, 675
Kraft, R. P., Forman, W. R., Jones, C., et al. 2002, ApJ, 569, 54
Kraft, R. P., Vázquez, S. E., Forman, W. R., et al. 2003, ApJ, 592, 129
Marston, A. P., & Dickens, R. J. 1988, A&A, 193, 27
Minniti, D., Rejkuba, M., Funes, J. G., & Akiyama, S. 2003, ApJ, 600, 716
Monet, D. G., Levine, S. E., Canzian, B., et al. 2003, AJ, 125, 984
Moretti, A., Campana, S., Lazzati, D., & Tagliaferri, G. 2003, ApJ, 588, 696
Morrison, J. E., Röser, S., McLean, B., Bucciarelli, B., & Lasker, B. 2001, AJ, 121, 1752
Peng, E. W., Ford, H. C., & Freeman, K. C. 2003, ApJS, 150, 367
Postnov, K. A., & Kuranov, A. G. 2005, Astro. Lett., 31, 7
Press, W. H., Teukolsky, S. A., Vetterling, W. T., & Flannery, B. P. 1992, Numerical recipes in C. The art of scientific computing (Cambridge: University Press)
Prestwich, A. H., Irwin, J. A., Kildgard, R. E., et al. 2003, ApJ, 595, 719
Roeser, S., Bastian, U., & Wiese, K. 1991, A&AS, 88, 277
Rosati, P., Tozzi, P., Giacconi, R., et al. 2002, ApJ, 556, 667
Schiminovich, D., van Gorkom, J. H., van der Hulst, J. M., & Kasow, S. 1994, ApJ, 423, L101
Shtykovskiy, P., & Gilfanov, M. 2005, A&A, 431, 597
Woodley, K. A., Harris, W. E., & Harris, G. L. H. 2005, AJ, 129, 2654

Online Material

Appendix A: Correction for incompleteness

The variations of the diffuse background level and deterioration of the point spread function at large off-axis angles lead to variations of the point-source sensitivity accross the Chandra images. In the case where several observations with different pointing directions are combined, this effect is further amplified by the non uniform exposure of the combined image. As a result, the completness of the source sample at the faint end is compromised. A trivial solution to this problem is to define a conservative sensitivity limit, which is high enough to be achieved everywhere across the image. Although simple in implementation, this method has a disadvantage that a noticeable fraction of the source has to be thrown away. Nevertheless, it has been used, with few exceptions (e.g. Kim & Fabbiano 2004; Shtykovskiy & Gilfanov 2005), in the majority of the earlier studies of the point source populations in galaxies. A more effective approach to the problem is to define the correction function to the flux/luminosity distribution, which accounts for the sensitivity variations accross the image. For a uniform distribution of sources this correction function simply accounts for the dependence of the survey area upon the energy flux or count rate. This is the case, for example, in the CXB studies. In a more complex case of a non-uniform distribution of point sources, the observed and real flux distributions are related via:

$$\left(\frac{\mathrm{d}N}{\mathrm{d}S}\right)_{\rm obs} = \int_{S_0\le S} \frac{\mathrm{d}N}{\mathrm{d}S}\,\Sigma(x,y)\,\mathrm{d}x\mathrm{d}y \qquad (A.1)$$

where $\Sigma(x,y)$ is the surface density distribution of point sources, and for given flux S the integration is performed over the part of the image where the local sensitivity $S_0(x,y)$ satisfies the condition $S_0(x,y) \le S$. If the flux distribution does not depend on the position, it can be easily recovered from the above equation. Importantly, knowledge of the spatial distribution of sources is required in order to recover the flux distribution and vice versa. If both flux and density distributions are unknown, the sample incompleteness can not be properly accounted for. The problem is further complicated by the contribution of the CXB sources, having a diferent spatial and flux distributions:

$$\left(\frac{\mathrm{d}N}{\mathrm{d}S}\right)_{\rm obs} = \int_{S_0\le S} \left(\frac{\mathrm{d}N}{\mathrm{d}S}\right)_{\rm LMXB} \Sigma_{\rm xrb}(x,y)\,\mathrm{d}x\mathrm{d}y + \int_{S_0\le S} \left(\frac{\mathrm{d}N}{\mathrm{d}S}\right)_{\rm CXB} \Sigma_{\rm cxb}(x,y)\,\mathrm{d}x\mathrm{d}y. \qquad (A.2)$$

For the practical implementation of the correction procedure, knowledge of the source detection algorithm is of course required. The `wavdetect` task (Freeman et al. 2002) correlates the image with a Mexican Hat function and registers sources with the correlation value exceeding a threshold value. The latter is estimated numerically based on the user-specified threshold significance. For each of the used detection scales we computed the threshold sensitivity on a grid of the positions on the image (16 azimuthal angles, 40 radii from the centre of Cen A). At each image position the PSF was obtained from the CALDB PSF library for each of the four individual observations and then combined with the exposure times as weights. The local background levels were found from the normalized background maps created by `wavdetect`. The sensitivity for any given position on the image was found from interpolation of the grid values. The sample incompleteness is described by the incompleteness function:

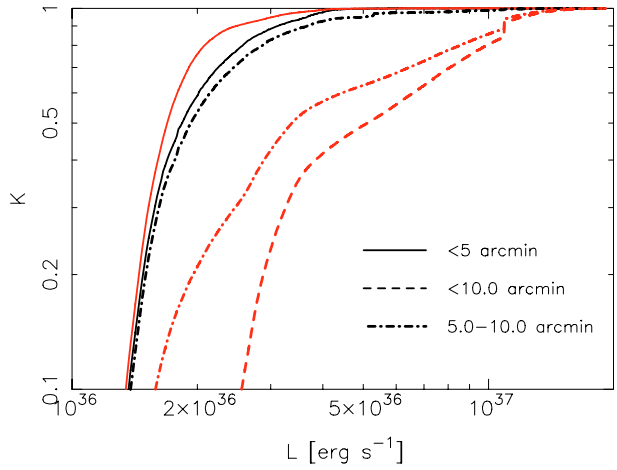

Fig. A.1. The sample incompleteness as a function of the luminosity for the inner (<5′), outer (5−10′) and full region. The black lines are calculated using the source density proportional to the K-band light distribution. The grey lines are calculated assuming a uniform source density.

$$K(L) = \sum_{L_0(i,j)\le L} \Sigma(i,j) \qquad (A.3)$$

where i, j are the pixel coordinates and $L_0(i,j)$ is the position-dependent sensitivity. Depending on the desired normalization of the $K(L)$, the the density distribution $\Sigma(i,j)$ can be normalized to unity or, for example, be given in the units of $M_\odot$ per pixel of the image.

If the CXB contribution can be neglected (Eq. (A.1)), the corrected luminosity distribution can be obtained giving the weight $1/K(L)$ to a source of luminosity L. For the ML fits the model should be multiplied by the $K(L)$.

For the general case of Eq. (A.2), the incompleteness function $K(L)$ should be calculated for the CXB and LMXB components separately. For the LMXBs density distribution we used the K-band image, the CXB distribution was assumed to be uniform. The corresponding incompleteness functions are shown in Fig. A.1. They demonstrate clearly importance of the spatial distribution of sources.

The results of one of our simulations are shown in Fig. A.2. In these simulations the background map from the `wavdetect` and the K-band image were azimutahlly averaged. The flux/luminosity distributions for the CXB sources and LMXBs were assumed in the form described in Sects. 4.3 and 4.4. In the simulations, the sources were randomly drawn from the assumed spatial and luminosity distributions and projected to the image using the PSF data from CALDB. The image of expectation values, containing the diffuse component and the point source contribution was then randomized assuming Poisson statistics. The final image was analysed using the same chain of tasks as applied to the real images. The simulated and obtained luminosity distributions are shown in Fig. A.2.

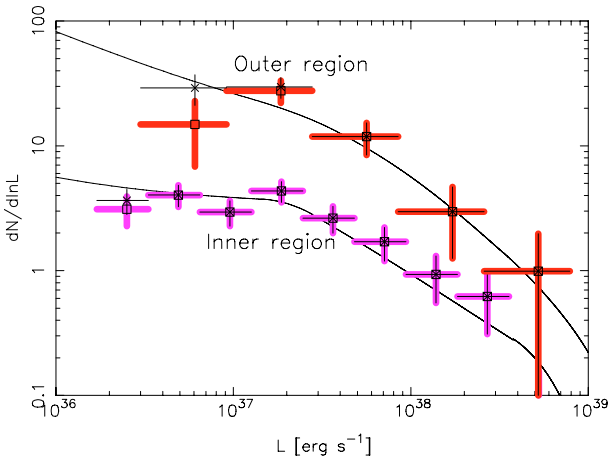

Fig. A.2. Simulated luminosity functions for the inner, $r \leq 5'$, and outer, $r \geq 5'$, regions. The input distributions (solid lines) are compared with the results obtained from the analysis of the images, done in the same way as the analysis of the real data. Both data corrected (asterisks) for incompleteness and uncorrected (squares) are shown. The normalization of the inner region has been divided by 10 for clarity.

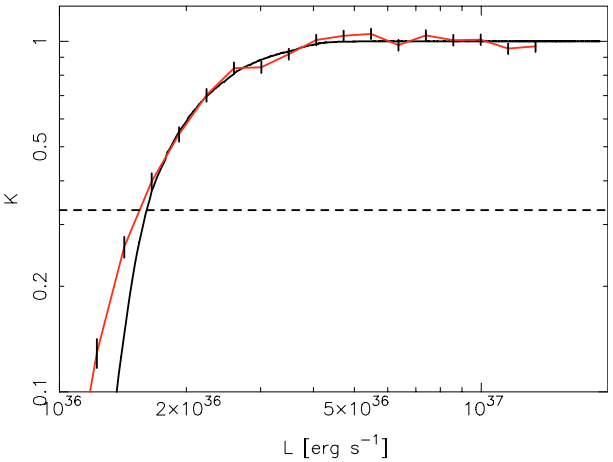

Fig. A.3. The incompleteness correction function for LMXBs within 5′ from the centre of Cen A. The solid line is the function used throughout this paper, whereas the red line is found using the backward correction method of Kim & Fabbiano (2003). The dashed line marks the correction limit. Sources with a correction larger than this are not included in the analyses carried out in this paper.

The Figs. A.1 and A.2 demonstrate that given the pattern of Chandra observations of Cen A, incompleteness effects are not of primary concern in the inner $r \lesssim 5'$ region at the luminosoties above $\sim(2{-}3) \times 10^{36}$ erg/s. They should be taken into account, however, for the source counts in the entire image and in the outer ring.

A.1. Verification of the incompleteness correction

Although simulations described above show that the correction procedure is adequate for the analysis of Cen A, their accuracy is limited by the Poisonian statistics. Such accuracy limitations are intrinsic to full simulations of individual galaxies because the number of sources thaimit can be put into a simulation is limited by the crowding effect. Another disadvantage of these simulation is that we used smoothed background maps produced by `wavdetect`, which, in addition, were azimuthally averaged.

In order to perform a more accurate and sensitive check of our incompleteness correction procedure we used a more direct, but also more computationally expensive, method, similar to the backward correction method suggested by Kim & Fabbiano (2003). In this method sources are placed one at a time on the real (unprocessed) observed image. For each simulated source the source detection and photometry are performed with the `wavdetect` task and then the original image is restored. As each source is put on the original undisturbed image, an arbitrarily large number of sources can be simulated. The incompleteness function is given by the source detection efficiency and can be computed as a ratio of the flux distribution of the detected sources to the input flux distribution.

Using this method we checked the incompleteness correction for the region within 5′ from the centre of Cen A, for the LMXB component. As above, the source distribution was assumed to follow the K-band light, and the differential luminosity function was chosen to follow $1/L$. The sources were put on the image using the same method as in the simulations above, utilizing the CALDB PSF library together with the exposure map of the observations. To reduce statistical errors, we simulated 20 000 sources.

The resulting incompleteness correction, together with the correction function utilized throughout this paper, is shown in Fig. A.3. As it can be seen from the figure, the two curves differ at low fluxes, corresponding to $L_X \lesssim 1.5 \times 10^{36}$ erg/s. The difference is caused by two effects. Firstly, the Eddington bias is neglected in our incompleteness correction calculations whereas it is automatically included in the simulations. The second reason is that in the `wavdetect` task the source detection and countrate calculation are based on two different calculations. The source detection uses the correlation values of the wavelet transform to determine the source significance, whereas the photometry is performed on the original image. Although there is a linear relation between the expectation values of the source countrate and wavelet correlation, the measured numbers are subject to statistical fluctuations. This is ignored in the correction procedure, which uses the wavelet correlation values to both calculate the source significance and source flux. This effect is only important at low numbers of counts, where only a few sources are detected. These weak sources are excluded from our luminosity function analysis as we include only sources with the detection efficiency of $\geq 1/3$. For the weakest source used to plot Figs. 5–7 the difference between two correction factors is 4.6%. In Fig. 7, for example, the lowest luminosity bin would decrease by ∼2%. This accuracy of the incompleteness correction is sufficient for the analysis presented in this paper.

Table A.1. The list of point like X-ray sources within $r < 10'$ from the center of Cen A.

ID	CXO Name	Dist	RA	Dec	Total Cts	Source Cts	Error	Luminosity	Type	ID reference
(1)	(2)	(3)	(4)	(5)	(6)	(7)	(8)	(9)	(10)	(11)
1	CXOU J132526.9-430052	17.5	13 25 27.0	–43 00 52.8	499	266.8	22.3	2.36×10^{37}		
2	CXOU J132529.1-430114	18.1	13 25 29.2	–43 01 14.6	219	78.8	14.8	7.17×10^{36}	H_α	mrfa-45
3	CXOU J132526.4-430054	19.1	13 25 26.5	–43 00 54.6	1905	1480.7	43.6	1.28×10^{38}		
4	CXOU J132526.7-430126	19.7	13 25 26.8	–43 01 26.1	523	267.1	22.9	2.29×10^{37}		
5	CXOU J132527.5-430128	19.8	13 25 27.5	–43 01 28.5	991	705.3	31.5	5.99×10^{37}	GC	mrfa-053
6	CXOU J132529.4-430108	20.2	13 25 29.5	–43 01 08.3	498	297.4	22.3	2.52×10^{37}	GC	mrfa-044
7	CXOU J132526.6-430129	23.3	13 25 26.6	–43 01 29.4	118	51.6	10.9	5.25×10^{36}		
8	CXOU J132525.7-430056	23.8	13 25 25.8	–43 00 56.1	1862	1578.1	43.2	1.35×10^{38}	GC	mrfa-017
9	CXOU J132525.2-430114	26.1	13 25 25.3	–43 01 14.3	105	61.7	10.2	6.03×10^{36}		
10	CXOU J132529.6-430122	26.4	13 25 29.7	–43 01 22.5	68	31.3	8.2	3.09×10^{36}		
11	CXOU J132525.5-430124	27.3	13 25 25.6	–43 01 24.2	259	110.3	16.1	9.66×10^{36}		
12	CXOU J132528.4-430137	30.6	13 25 28.5	–43 01 37.9	96	42.9	9.8	4.01×10^{36}		
13	CXOU J132525.1-430127	32.3	13 25 25.2	–43 01 27.1	741	565.7	27.2	4.90×10^{37}	GC	mrfa-057
14	CXOU J132524.7-430125	34.9	13 25 24.8	–43 01 25.0	263	181.6	16.2	1.66×10^{37}		
15	CXOU J132524.3-430110	35.8	13 25 24.4	–43 01 10.4	199	121.7	14.1	1.09×10^{37}		
16	CXOU J132527.0-430030	38.7	13 25 27	–43 00 30.6	172	128.5	13.1	1.15×10^{37}		
17	CXOU J132530.8-430128	40.5	13 25 30.9	–43 01 28.4	67	37.4	8.2	3.54×10^{36}		
18	CXOU J132523.9-430059	41.5	13 25 23.9	–43 00 59.0	312	227.5	17.7	2.00×10^{37}		
19	CXOU J132531.4-430057	43.9	13 25 31.5	–43 00 57.2	38	21.6	6.2	2.05×10^{36}		
20	CXOU J132523.8-430127	45.2	13 25 23.9	–43 01 27.2	61	31.1	7.8	3.24×10^{36}		
21	CXOU J132524.4-430141	47.6	13 25 24.4	–43 01 41.2	252	168.2	15.9	1.51×10^{37}	H_α	mrfa-60
22	CXOU J132527.0-430159	50.9	13 25 27.1	–43 01 59.4	825	675.6	28.7	5.76×10^{37}	H_α	mrfa-54
23	CXOU J132527.2-430016	52.9	13 25 27.3	–43 00 16.0	35	21.2	5.9	2.23×10^{36}		
24	CXOU J132524.1-430145	53.0	13 25 24.2	–43 01 45.7	84	49.3	9.2	4.74×10^{36}		
25	CXOU J132523.3-430043	53.1	13 25 23.4	–43 00 43.6	79	48.2	8.9	4.61×10^{36}		
26	CXOU J132523.5-430138	53.9	13 25 23.5	–43 01 38.7	714	589.2	26.7	5.15×10^{37}		
27	CXOU J132522.9-430125	54.2	13 25 22.9	–43 01 25.1	1947	1780	44.1	1.53×10^{38}		
28	CXOU J132523.0-430134	56.1	13 25 23.1	–43 01 34.9	226	157.3	15	1.46×10^{37}		
29	CXOU J132532.4-430134	58.9	13 25 32.5	–43 01 34.3	869	768.3	29.5	6.41×10^{37}		
30	CXOU J132522.3-430122	59.1	13 25 22.4	–43 01 22.3	63	33.8	7.9	3.37×10^{36}		
31	CXOU J132533.0-430108	59.9	13 25 33.1	–43 01 08.0	264	213.4	16.2	1.80×10^{37}		
32	CXOU J132523.0-430145	61.9	13 25 23.1	–43 01 45.8	406	312.7	20.2	2.77×10^{37}		
33	CXOU J132526.9-430004	64.4	13 25 26.9	–43 00 04.9	25	18.5	5.0	4.84×10^{36}		
34	CXOU J132522.1-430132	65.0	13 25 22.1	–43 01 32.3	85	59.1	9.2	6.00×10^{36}		
35	CXOU J132533.3-430053	65.0	13 25 33.4	–43 00 53.1	507	427.8	22.5	3.64×10^{37}	H_α	mrfa-06
36	CXOU J132525.5-430210	65.5	13 25 25.6	–43 02 10.5	63	46	7.9	4.54×10^{36}	GC	mrfa-055
37	CXOU J132527.4-430214	65.5	13 25 27.5	–43 02 14.3	1609	1496.2	40.1	1.27×10^{38}		
38	CXOU J132531.3-430203	68.2	13 25 31.4	–43 02 03.3	22	18.8	4.7	1.74×10^{37}		
39	CXOU J132527.6-430218	69.4	13 25 27.7	–43 02 18.2	288	227.8	17	1.98×10^{37}	FS	mrfa-51
40	CXOU J132521.3-430046	72.1	13 25 21.4	–43 00 46.0	51	36.9	7.1	3.72×10^{36}		
41	CXOU J132522.8-430017	72.9	13 25 22.9	–43 00 17.6	363	331.7	19.1	3.02×10^{37}		
42	CXOU J132523.7-430009	73.0	13 25 23.7	–43 00 09.7	1835	1730	42.8	1.50×10^{38}	H_α	mrfa-21
43	CXOU J132524.7-430002	73.2	13 25 24.8	–43 00 02.6	116	85.4	10.8	7.40×10^{36}		
44	CXOU J132524.2-425959	78.5	13 25 24.2	–42 59 59.7	573	521.5	23.9	4.55×10^{37}	H_α	mrfa-19
45	CXOU J132525.3-430223	78.8	13 25 25.3	–43 02 23.4	213	180.1	14.6	1.63×10^{37}		
46	CXOU J132521.7-430154	78.8	13 25 21.7	–43 01 54.2	191	137.5	13.8	1.22×10^{37}		
47	CXOU J132531.6-430003	78.9	13 25 31.6	–43 00 03.3	1023	962.6	32	8.08×10^{37}	GC	pff-gc-210
48	CXOU J132528.7-425948	81.2	13 25 28.8	–42 59 48.6	1107	1034.7	33.3	8.67×10^{37}		
49	CXOU J132521.2-430154	83.9	13 25 21.2	–43 01 55.0	212	189	14.6	1.78×10^{37}		
50	CXOU J132523.5-430220	84.4	13 25 23.6	–43 02 20.8	465	421	21.6	3.73×10^{37}		
51	CXOU J132521.2-430158	85.5	13 25 21.3	–43 01 58.9	223	174.4	14.9	1.54×10^{37}		
52	CXOU J132521.5-430213	93.0	13 25 21.6	–43 02 13.8	146	124.7	12.1	1.15×10^{37}		
53	CXOU J132520.8-430010	94.3	13 25 20.8	–43 00 10.8	27	20.3	5.2	2.11×10^{36}		
54	CXOU J132532.0-430231	95.8	13 25 32.0	–43 02 31.5	535	490.7	23.1	4.17×10^{37}	H_α	mrfa-40
55	CXOU J132525.8-425933	97.4	13 25 25.8	–42 59 33.4	33	17.4	5.7	1.61×10^{36}		
56	CXOU J132530.3-425935	98.1	13 25 30.3	–42 59 35.2	136	89.8	11.7	7.58×10^{36}	GC	pff-gc-209
57	CXOU J132518.9-430136	98.7	13 25 19.0	–43 01 37.0	67	48.6	8.2	4.81×10^{36}		
58	CXOU J132529.0-425931	98.9	13 25 29.0	–42 59 31.1	95	59.8	9.7	5.10×10^{36}		

Table A.1. continued.

ID	CXO Name	Dist	RA	Dec	Total Cts	Source Cts	Error	Luminosity	Type	ID reference
(1)	(2)	(3)	(4)	(5)	(6)	(7)	(8)	(9)	(10)	(11)
59	CXOU J132536.6-430057	99.5	13 25 36.6	–43 00 57.6	303	233.9	17.4	1.94×10^{37}		
60	CXOU J132518.5-430116	99.8	13 25 18.5	–43 01 16.3	578	523.1	24	4.58×10^{37}	GC	mrfa-074
61	CXOU J132519.9-430203	100.4	13 25 19.9	–43 02 03.3	38	25	6.2	2.69×10^{36}		
62	CXOU J132518.7-430141	102.7	13 25 18.7	–43 01 41.2	96	72.3	9.8	7.04×10^{36}		
63	CXOU J132519.2-430158	104.6	13 25 19.2	–43 01 58.4	61	45.1	7.8	5.07×10^{36}		
64	CXOU J132528.2-430253	105.0	13 25 28.2	–43 02 53.6	368	340.1	19.2	2.98×10^{37}		
65	CXOU J132537.4-430131	110.2	13 25 37.4	–43 01 31.8	109	81.5	10.4	6.81×10^{36}	GC	mrfa-033
66	CXOU J132526.7-430300	112.0	13 25 26.8	–43 03 00.4	188	159.4	13.7	1.40×10^{37}		
67	CXOU J132518.7-430205	113.2	13 25 18.7	–43 02 05.8	41	27.3	6.4	2.88×10^{36}		
68	CXOU J132522.2-430245	113.7	13 25 22.2	–43 02 45.8	126	116.9	11.2	1.09×10^{37}	GC	pff-gc-121
69	CXOU J132520.6-425942	115.5	13 25 20.7	–42 59 42.1	22	12.7	4.7	1.30×10^{36}		
70	CXOU J132530.4-425914	118.7	13 25 30.5	–42 59 14.3	496	435.8	22.3	3.68×10^{37}		
71	CXOU J132535.2-430234	119.4	13 25 35.2	–43 02 34.1	150	120.8	12.2	1.03×10^{37}		
72	CXOU J132517.8-430204	120.4	13 25 17.9	–43 02 04.4	209	181.6	14.5	2.10×10^{37}		
73	CXOU J132531.9-430302	123.1	13 25 31.9	–43 03 02.5	56	38.2	7.5	3.34×10^{36}		
74	CXOU J132527.8-425903	125.0	13 25 27.9	–42 59 03.9	43	26.5	6.6	2.35×10^{36}		
75	CXOU J132528.4-430315	126.9	13 25 28.4	–43 03 15.4	251	211.5	15.8	1.81×10^{37}		
76	CXOU J132535.5-425935	127.6	13 25 35.5	–42 59 35.3	609	549	24.7	5.27×10^{37}	GC	pff-gc-214
77	CXOU J132538.3-430205	130.4	13 25 38.3	–43 02 05.8	2221	2158.8	47.1	1.78×10^{38}		
78	CXOU J132539.4-430058	130.6	13 25 39.5	–43 00 58.9	39	22	6.2	1.99×10^{36}		
79	CXOU J132517.0-430007	131.1	13 25 17.1	–43 00 07.5	46	33.9	6.8	3.15×10^{36}		
80	CXOU J132533.3-425913	131.5	13 25 33.4	–42 59 13.6	101	78	10.1	7.40×10^{36}		
81	CXOU J132515.7-430158	139.6	13 25 15.7	–43 01 58.2	58	44.7	7.6	7.11×10^{36}		
82	CXOU J132533.6-430313	141.2	13 25 33.7	–43 03 13.3	188	159.3	13.7	1.36×10^{37}		
83	CXOU J132514.8-430048	141.6	13 25 14.8	–43 00 48.7	42	21.3	6.5	1.94×10^{36}		
84	CXOU J132540.5-430115	142.1	13 25 40.6	–43 01 15.2	638	587	25.3	5.02×10^{37}		
85	CXOU J132538.2-430230	142.3	13 25 38.3	–43 02 30.5	15	9.4	3.9	9.11×10^{35}		
86	CXOU J132523.6-430325	143.9	13 25 23.6	–43 03 25.9	256	221.8	16	2.38×10^{37}		
87	CXOU J132533.9-425859	146.4	13 25 34.0	–42 58 59.9	558	514.4	23.6	4.59×10^{37}	GC	pff-gc-159
88	CXOU J132520.0-430310	147.1	13 25 20.1	–43 03 10.4	367	317.4	19.2	3.95×10^{37}	GC	mrfa-071
89	CXOU J132516.9-425938	147.9	13 25 16.9	–42 59 38.8	19	11.9	4.4	1.18×10^{36}		
90	CXOU J132532.4-425850	148.1	13 25 32.4	–42 58 50.5	206	180.8	14.4	1.80×10^{37}	GC	pff-gc-178
91	CXOU J132522.3-425852	148.2	13 25 22.4	–42 58 52.2	41	25.8	6.4	2.34×10^{36}		
92	CXOU J132541.0-430126	148.6	13 25 41.1	–43 01 26.8	607	574.2	24.6	4.95×10^{37}		
93	CXOU J132514.0-430121	149.6	13 25 14.0	–43 01 21.6	63	43.4	7.9	6.44×10^{36}		
94	CXOU J132541.0-430037	150.0	13 25 41.0	–43 00 37.7	49	25.6	7	2.21×10^{36}		
95	CXOU J132516.8-425932	152.7	13 25 16.8	–42 59 32.4	34	24.3	5.8	2.29×10^{36}		
96	CXOU J132519.9-430317	153.5	13 25 19.9	–43 03 17.2	2263	2028.1	47.6	2.10×10^{38}		
97	CXOU J132524.9-430341	155.2	13 25 24.9	–43 03 41.2	33	22.8	5.7	2.46×10^{36}		
98	CXOU J132527.3-425829	159.2	13 25 27.3	–42 58 29.7	68	48.3	8.2	4.29×10^{36}		
99	CXOU J132541.9-430142	161.0	13 25 42.0	–43 01 42.3	32	21.7	5.7	1.98×10^{36}		
100	CXOU J132512.9-430114	161.4	13 25 12.9	–43 01 14.7	589	527.1	24.3	7.40×10^{37}	GC	mrfa-082
101	CXOU J132520.6-425846	162.2	13 25 20.6	–42 58 46.0	712	676.3	26.7	6.04×10^{37}		
102	CXOU J132516.4-430255	162.5	13 25 16.4	–43 02 55.4	290	262.1	17	3.19×10^{37}		
103	CXOU J132538.6-425919	162.5	13 25 38.6	–42 59 20.0	99	70.5	10	6.21×10^{36}	GC	pff-gc-164
104	CXOU J132512.4-430049	167.4	13 25 12.5	–43 00 49.4	56	39.5	7.5	5.09×10^{36}		
105	CXOU J132512.0-430044	172.7	13 25 12.0	–43 00 44.6	343	302.3	18.5	3.73×10^{37}		
106	CXOU J132540.0-430255	173.2	13 25 40.1	–43 02 55.5	45	27.1	6.7	2.34×10^{36}		
107	CXOU J132527.9-430402	173.7	13 25 28.0	–43 04 02.5	194	167.4	13.9	1.47×10^{37}	GC	mrfa-050
108	CXOU J132540.4-430251	174.4	13 25 40.5	–43 02 51.8	38	26.7	6.2	2.37×10^{36}	H_α	mrfa-30
109	CXOU J132540.8-430247	175.0	13 25 40.8	–43 02 47.1	267	234.5	16.3	1.97×10^{37}		
110	CXOU J132514.0-430243	175.8	13 25 14.1	–43 02 43.2	141	118.9	11.9	1.29×10^{37}	GC	mrfa-080
111	CXOU J132535.7-430340	176.5	13 25 35.8	–43 03 40.9	44	33.7	6.6	3.06×10^{36}		
112	CXOU J132512.0-430010	180.6	13 25 12.0	–43 00 11.0	473	441.9	21.7	3.99×10^{37}	FS	mrfa-85
113	CXOU J132529.4-425809	180.6	13 25 29.4	–42 58 09.3	28	18	5.3	1.96×10^{36}	GC	pff-gc-155
114	CXOU J132533.8-425821	180.8	13 25 33.9	–42 58 21.5	78	61.6	8.8	5.72×10^{36}		
115	CXOU J132511.1-430132	182.7	13 25 11.1	–43 01 32.3	25	17.8	5	2.54×10^{36}		

Table A.1. continued.

ID	CXO Name	Dist	RA	Dec	Total Cts	Source Cts	Error	Luminosity	Type	ID reference
(1)	(2)	(3)	(4)	(5)	(6)	(7)	(8)	(9)	(10)	(11)
116	CXOU J132542.7-425943	186.6	13 25 42.8	–42 59 43.9	28	17.3	5.3	1.60×10^{36}		
117	CXOU J132528.3-430416	187.9	13 25 28.3	–43 04 16.5	113	95.9	10.6	8.55×10^{36}		
118	CXOU J132511.5-430226	192.1	13 25 11.6	–43 02 26.6	184	161.9	13.6	1.74×10^{37}		
119	CXOU J132514.5-425858	193.9	13 25 14.5	–42 58 58.7	22	13.7	4.7	1.37×10^{36}		
120	CXOU J132517.7-430350	194.4	13 25 17.8	–43 03 50.6	43	29.9	6.6	3.45×10^{36}		
121	CXOU J132545.6-430115	197.9	13 25 45.7	–43 01 15.9	79	43.1	8.9	3.62×10^{36}	GAL	whh-317
122	CXOU J132524.9-430425	199.1	13 25 24.9	–43 04 25.7	151	132.9	12.3	1.58×10^{37}		
123	CXOU J132512.1-425918	201.8	13 25 12.2	–42 59 18.8	34	25.3	5.8	2.57×10^{36}		
124	CXOU J132529.3-425747	201.8	13 25 29.3	–42 57 47.8	48	23.8	6.9	2.18×10^{36}	GC	whh-22
125	CXOU J132514.8-425840	204.1	13 25 14.8	–42 58 40.8	33	23.2	5.7	2.23×10^{36}		
126	CXOU J132542.1-430319	206.0	13 25 42.1	–43 03 20.0	52	30.5	7.2	2.59×10^{36}	GC	mrfa-026
127	CXOU J132538.2-425815	208.6	13 25 38.2	–42 58 15.8	131	107	11.4	9.14×10^{36}	GC	mrfa-003
128	CXOU J132532.8-430429	208.8	13 25 32.9	–43 04 29.4	173	146.6	13.2	1.30×10^{37}		
129	CXOU J132546.4-430036	209.2	13 25 46.5	–43 00 36.7	54	31.1	7.3	2.82×10^{36}		
130	CXOU J132519.0-425759	211.5	13 25 19.1	–42 57 59.3	55	42.9	7.4	4.28×10^{36}		
131	CXOU J132524.4-425735	216.1	13 25 24.4	–42 57 35.6	12	7.1	3.5	2.08×10^{36}		
132	CXOU J132513.1-425841	216.5	13 25 13.2	–42 58 41.2	23	17.2	4.8	1.93×10^{36}		
133	CXOU J13257.82-430059	217.3	13 25 07.8	–43 00 59.8	24	15.9	4.9	2.06×10^{36}		
134	CXOU J132532.3-430441	218.7	13 25 32.3	–43 04 41.3	49	34.3	7.0	3.27×10^{36}		
135	CXOU J132507.6-430115	219.1	13 25 07.7	–43 01 15.5	2028	1873	45.0	1.90×10^{38}	GC	whh-8
136	CXOU J132516.0-430411	222.1	13 25 16.0	–43 04 11.1	31	17.2	5.6	2.14×10^{36}		
137	CXOU J132547.6-430030	223.0	13 25 47.7	–43 00 30.7	89	45	9.4	4.18×10^{36}		
138	CXOU J132543.2-425837	228.5	13 25 43.2	–42 58 37.6	152	120.9	12.3	1.04×10^{37}	GC	pff-gc-062
139	CXOU J132509.3-425917	229.0	13 25 09.4	–42 59 17.6	78	45.4	8.8	4.13×10^{36}		
140	CXOU J132521.8-430451	231.3	13 25 21.8	–43 04 51.2	120	70.1	11	7.33×10^{36}		
141	CXOU J132512.0-425830	233.2	13 25 12.0	–42 58 30.7	63	33.6	7.9	3.02×10^{36}		
142	CXOU J132512.3-425824	234.6	13 25 12.3	–42 58 24.5	82	56.4	9.1	5.12×10^{36}		
143	CXOU J132547.1-430243	234.7	13 25 47.2	–43 02 43.6	181	151.7	13.5	1.32×10^{37}		
144	CXOU J132514.8-430418	235.4	13 25 14.8	–43 04 18.0	89	35.8	9.4	3.89×10^{36}		
145	CXOU J132538.8-430432	237.9	13 25 38.9	–43 04 32.1	32	17.5	5.7	1.63×10^{36}		
146	CXOU J132522.3-425717	238.4	13 25 22.4	–42 57 17.4	914	845.7	30.2	7.37×10^{37}	GC	mrfa-208
147	CXOU J132546.3-430310	239.1	13 25 46.4	–43 03 10.8	406	356.8	20.1	3.35×10^{37}	FS	mrfa-93
148	CXOU J132509.2-425859	239.7	13 25 09.2	–42 58 59.5	682	594	26.1	5.21×10^{37}	GC	mrfa-215
149	CXOU J132506.3-430221	244.4	13 25 06.3	–43 02 21.2	974	818.5	31.2	8.26×10^{37}		
150	CXOU J132515.8-425739	245.6	13 25 15.8	–42 57 39.9	141	106.5	11.9	9.78×10^{36}		
151	CXOU J132505.0-430133	248.9	13 25 05.0	–43 01 33.5	292	239.9	17.1	2.51×10^{37}		
152	CXOU J132534.2-425709	249.9	13 25 34.3	–42 57 09.7	47	25.2	6.9	2.46×10^{36}		
153	CXOU J132547.6-425903	252.6	13 25 47.6	–42 59 03.8	56	36.4	7.5	3.31×10^{36}		
154	CXOU J132529.2-430521	253.4	13 25 29.2	–43 05 21.5	32	19.4	5.7	3.10×10^{36}		
155	CXOU J132548.5-430258	254.6	13 25 48.6	–43 02 58.4	33	18.8	5.7	2.02×10^{36}		
156	CXOU J132527.5-430525	256.5	13 25 27.6	–43 05 25.3	55	37.2	7.4	4.92×10^{36}		
157	CXOU J132538.5-425720	258.0	13 25 38.6	–42 57 20.5	102	57.5	10.1	5.36×10^{36}		
158	CXOU J132518.8-425708	258.7	13 25 18.9	–42 57 08.5	91	61.5	9.5	6.02×10^{36}		
159	CXOU J132523.5-425651	260.7	13 25 23.5	–42 56 52.0	204	170.4	14.3	1.78×10^{37}		
160	CXOU J132504.4-430008	261.5	13 25 04.4	–43 00 08.2	94	69.8	9.7	7.71×10^{36}		
161	CXOU J132545.5-425815	261.7	13 25 45.5	–42 58 15.9	242	179.5	15.6	1.73×10^{37}		
162	CXOU J132533.6-430525	265.1	13 25 33.7	–43 05 25.4	86	63.8	9.3	8.22×10^{36}	FS	HD 116647 fs
163	CXOU J132548.5-430322	265.6	13 25 48.5	–43 03 22.8	56	41.8	7.5	5.83×10^{36}		
164	CXOU J132539.8-430501	268.9	13 25 39.8	–43 05 01.9	100	86.8	10	2.20×10^{37}	GC	pff-gc-111
165	CXOU J132547.2-425825	270.0	13 25 47.2	–42 58 25.6	179	139.7	13.4	1.22×10^{37}		
166	CXOU J132538.0-430513	270.4	13 25 38.1	–43 05 13.6	98	82.2	9.9	2.00×10^{37}		
167	CXOU J132526.1-425636	272.5	13 25 26.2	–42 56 36.7	184	139.6	13.6	1.25×10^{37}		
168	CXOU J132549.4-425858	273.2	13 25 49.5	–42 58 58.4	34	16.6	5.8	1.62×10^{36}		
169	CXOU J132535.2-430529	273.3	13 25 35.2	–43 05 29.0	18	14.2	4.2	4.67×10^{36}	GC	whh-17
170	CXOU J132527.5-430549	281.1	13 25 27.6	–43 05 49.9	59	35.1	7.7	4.60×10^{36}		
171	CXOU J132503.5-425928	282.5	13 25 03.5	–42 59 28.8	29	17.2	5.4	2.36×10^{36}		

Table A.1. continued.

ID	CXO Name	Dist	RA	Dec	Total Cts	Source Cts	Error	Luminosity	Type	ID reference
(1)	(2)	(3)	(4)	(5)	(6)	(7)	(8)	(9)	(10)	(11)
172	CXOU J132539.1-425654	284.3	13 25 39.1	–42 56 54.0	352	297.3	18.8	2.67×10^{37}		
173	CXOU J132507.4-430409	285.5	13 25 07.5	–43 04 09.3	6878	6474.7	82.9	6.69×10^{38}	FS	Kraft
174	CXOU J132553.5-430134	285.7	13 25 53.6	–43 01 34.9	73	44.4	8.5	3.95×10^{36}		
175	CXOU J132546.7-425752	287.1	13 25 46.7	–42 57 52.6	90	40.5	9.5	3.51×10^{36}		
176	CXOU J132502.7-430243	289.0	13 25 02.7	–43 02 43.5	2412	2257.9	49.1	2.45×10^{38}		
177	CXOU J132532.7-425624	290.1	13 25 32.8	–42 56 24.2	165	115.8	12.8	1.01×10^{37}	GC	pff-gc-056
178	CXOU J132512.0-425713	291.2	13 25 12.0	–42 57 13.3	29	21.9	5.4	9.13×10^{36}		
179	CXOU J132555.1-430119	301.8	13 25 55.1	–43 01 19.2	198	153.7	14.1	1.31×10^{37}		
180	CXOU J132538.4-425630	302.2	13 25 38.4	–42 56 30.8	150	100.3	12.2	8.94×10^{36}		
181	CXOU J132520.2-425615	304.3	13 25 20.3	–42 56 15.4	42	32.2	6.5	1.02×10^{37}		
182	CXOU J132552.2-425830	312.9	13 25 52.2	–42 58 30.7	71	21.6	8.4	1.86×10^{36}	GC	pff-gc-072
183	CXOU J132554.6-425925	313.4	13 25 54.6	–42 59 25.8	1500	1311.5	38.7	1.10×10^{38}	GC	pff-gc-131
184	CXOU J132549.7-430430	315.7	13 25 49.8	–43 04 30.3	26	18.5	5.1	5.02×10^{36}		
185	CXOU J132556.8-430044	321.8	13 25 56.9	–43 00 44.8	319	244.3	17.9	2.07×10^{37}		
186	CXOU J132546.5-425703	321.8	13 25 46.6	–42 57 03.4	638	487.2	25.3	4.56×10^{37}	GC	pff-gc-168
187	CXOU J132549.1-430447	321.9	13 25 49.2	–43 04 47.3	60	37.2	7.7	8.91×10^{36}		
188	CXOU J132508.2-430511	322.2	13 25 08.3	–43 05 11.3	364	189.8	19.1	2.11×10^{37}		
189	CXOU J132509.5-430529	327.5	13 25 09.6	–43 05 29.6	538	418.6	23.2	4.66×10^{37}		
190	CXOU J132534.4-425549	327.6	13 25 34.5	–42 55 49.8	239	164.9	15.5	1.48×10^{37}		
191	CXOU J132518.5-425547	336.0	13 25 18.6	–42 55 47.8	10	6.4	3.2	3.11×10^{36}		
192	CXOU J132553.4-425806	336.9	13 25 53.4	–42 58 06.5	106	40.4	10.3	3.50×10^{36}		
193	CXOU J132512.8-430606	338.8	13 25 12.9	–43 06 06.6	43	25.1	6.6	3.07×10^{36}		
194	CXOU J132547.3-425647	339.5	13 25 47.4	–42 56 47.4	144	70.8	12	6.87×10^{36}		
195	CXOU J132539.4-425546	347.6	13 25 39.4	–42 55 46.3	94	38.9	9.7	3.44×10^{36}		
196	CXOU J132543.9-430610	350.1	13 25 43.9	–43 06 10.0	146	132.4	12.1	5.91×10^{37}		
197	CXOU J132507.7-425630	353.6	13 25 07.7	–42 56 30.5	70	56.3	8.4	2.80×10^{37}	GC	mrfa-216
198	CXOU J132510.1-425608	356.5	13 25 10.2	–42 56 08.0	39	30.2	6.2	1.61×10^{37}		
199	CXOU J132545.2-425604	360.4	13 25 45.2	–42 56 04.5	95	31	9.7	2.90×10^{36}		
200	CXOU J132456.1-430258	362.3	13 24 56.1	–43 02 59.0	144	80.9	12	1.09×10^{37}		
201	CXOU J132557.2-425822	364.8	13 25 57.2	–42 58 22.3	414	291.8	20.3	3.12×10^{37}		
202	CXOU J132510.6-430624	366.3	13 25 10.7	–43 06 24.5	398	299.5	20	3.28×10^{37}		
203	CXOU J132522.7-425502	370.6	13 25 22.7	–42 55 02.1	109	92	10.4	4.22×10^{37}		
204	CXOU J132601.4-430043	372.3	13 26 01.5	–43 00 43.5	109	37.9	10.4	3.32×10^{36}		
205	CXOU J132554.6-425720	374.0	13 25 54.6	–42 57 20.8	38	16.1	6.2	2.15×10^{36}		
206	CXOU J132531.4-430720	374.2	13 25 31.4	–43 07 20.7	33	26.6	5.7	1.24×10^{37}		
207	CXOU J132529.1-425447	381.9	13 25 29.2	–42 54 47.3	22	15.5	4.7	6.89×10^{36}		
208	CXOU J132545.2-425530	389.6	13 25 45.2	–42 55 30.6	96	36.9	9.8	3.92×10^{36}		
209	CXOU J132552.6-430545	389.6	13 25 52.6	–43 05 45.5	45	38.1	6.7	1.79×10^{37}	GC	pff-gc-129
210	CXOU J132503.1-425625	390.5	13 25 03.1	–42 56 25.5	43	29	6.6	1.43×10^{37}	GC	pff-gc-157
211	CXOU J132557.2-430450	393.1	13 25 57.2	–43 04 50.5	68	44.2	8.2	1.05×10^{37}		
212	CXOU J132558.6-430430	395.6	13 25 58.7	–43 04 30.4	1259	1180.4	35.5	2.69×10^{38}		
213	CXOU J132510.0-430655	396.1	13 25 10.1	–43 06 55.1	137	90.2	11.7	1.22×10^{37}		
214	CXOU J132529.0-430744	396.2	13 25 29.0	–43 07 44.7	23	16.5	4.8	7.34×10^{36}		
215	CXOU J132549.6-430624	397.9	13 25 49.7	–43 06 24.7	18	10.5	4.2	4.58×10^{36}		
216	CXOU J132510.2-425510	405.4	13 25 10.3	–42 55 10.8	80	65	8.9	3.34×10^{37}		
217	CXOU J132513.9-430725	405.7	13 25 14	–43 07 25.9	222	168.2	14.9	2.72×10^{37}		
218	CXOU J132548.7-425530	409.8	13 25 48.8	–42 55 31.0	76	47.7	8.7	1.05×10^{37}		
219	CXOU J132557.8-425702	413.6	13 25 57.9	–42 57 02.5	393	296.1	19.8	4.21×10^{37}		
220	CXOU J132521.2-425413	420.9	13 25 21.3	–42 54 13.7	113	98.8	10.6	4.82×10^{37}		
221	CXOU J132606.3-430112	424.8	13 26 06.4	–43 01 12.3	35	19.7	5.9	5.82×10^{36}		
222	CXOU J132545.4-425451	424.9	13 25 45.4	–42 54 51.4	119	80.3	10.9	1.69×10^{37}		
223	CXOU J132533.2-430810	426.3	13 25 33.2	–43 08 10.6	38	28.1	6.2	1.25×10^{37}		
224	CXOU J132522.7-430822	436.7	13 25 22.7	–43 08 22.2	20	13.3	4.5	6.24×10^{36}		
225	CXOU J132501.0-430643	443.8	13 25 01.1	–43 06 43.8	971	853	31.2	1.16×10^{38}		
226	CXOU J132511.1-430755	445.1	13 25 11.2	–43 07 55.9	144	101.4	12	1.48×10^{37}		

Table A.1. continued.

ID	CXO Name	Dist	RA	Dec	Total Cts	Source Cts	Error	Luminosity	Type	ID reference
(1)	(2)	(3)	(4)	(5)	(6)	(7)	(8)	(9)	(10)	(11)
227	CXOU J132506.8-430736	449.7	13 25 06.8	–43 07 36.5	86	43.1	9.3	6.10×10^{36}		
228	CXOU J132601.2-430528	450.3	13 26 01.2	–43 05 28.0	949	919.9	30.8	4.14×10^{38}		
229	CXOU J132544.1-430804	453.4	13 25 44.1	–43 08 04.5	146	135.7	12.1	6.92×10^{37}		
230	CXOU J132540.4-430820	453.7	13 25 40.5	–43 08 20.1	18	11	4.2	5.37×10^{36}		
231	CXOU J132550.3-425441	460.3	13 25 50.3	–42 54 41.9	82	34.4	9.1	4.82×10^{36}		
232	CXOU J132459.0-430648	462.6	13 24 59.0	–43 06 48.9	74	34.9	8.6	4.96×10^{36}		
233	CXOU J132450.4-430452	464.9	13 24 50.4	–43 04 52.3	106	55.9	10.3	7.67×10^{36}		
234	CXOU J132557.5-425531	470.6	13 25 57.5	–42 55 31.5	73	38.2	8.5	5.28×10^{36}		
235	CXOU J132504.0-425431	474.2	13 25 04	–42 54 31.5	107	44.1	10.3	6.57×10^{36}		
236	CXOU J132609.9-430310	479.6	13 26 09.9	–43 03 10.5	32	17.3	5.7	4.32×10^{36}		
237	CXOU J132557.5-430659	479.6	13 25 57.5	–43 06 59.2	23	16.7	4.8	8.07×10^{36}		
238	CXOU J132513.9-425331	481.3	13 25 13.9	–42 53 31.5	344	283.6	18.5	4.18×10^{37}		
239	CXOU J132548.1-430817	483.9	13 25 48.1	–43 08 17.2	43	29.7	6.6	1.35×10^{37}		
240	CXOU J132511.3-430843	488.6	13 25 11.3	–43 08 43.5	51	34.2	7.1	1.11×10^{37}		
241	CXOU J132542.0-425323	491.9	13 25 42.0	–42 53 23.1	26	16.6	5.1	8.55×10^{36}		
242	CXOU J132510.3-425333	493.4	13 25 10.4	–42 53 33.2	415	334.4	20.4	4.92×10^{37}		
243	CXOU J132611.8-430242	494.0	13 26 11.9	–43 02 42.9	280	247	16.7	6.45×10^{37}		
244	CXOU J132535.1-425301	494.1	13 25 35.2	–42 53 01.7	246	233.2	15.7	1.04×10^{38}		
245	CXOU J132546.7-425340	495.2	13 25 46.7	–42 53 40.1	209	118.5	14.5	1.64×10^{37}		
246	CXOU J132502.9-425413	496.3	13 25 02.9	–42 54 13.2	307	211.7	17.5	3.10×10^{37}		
247	CXOU J132605.5-425632	499.4	13 26 05.5	–42 56 32.5	191	132.7	13.8	1.89×10^{37}	GC	pff-gc-122
248	CXOU J132555.4-430745	500.7	13 25 55.5	–43 07 45.8	29	20.6	5.4	9.29×10^{36}		
249	CXOU J132614.1-430208	513.4	13 26 14.1	–43 02 08.6	73	55.6	8.5	2.84×10^{37}		
250	CXOU J132511.0-425257	523.7	13 25 11.0	–42 52 57.8	50	26.5	7.1	4.44×10^{36}		
251	CXOU J132527.3-430953	524.3	13 25 27.3	–43 09 53.1	61	48	7.8	2.21×10^{37}		
252	CXOU J132458.9-430831	542.7	13 24 58.9	–43 08 31.3	167	86.8	12.9	1.33×10^{37}		
253	CXOU J132456.7-430813	543.0	13 24 56.8	–43 08 13.7	798	594.6	28.3	8.36×10^{37}		
254	CXOU J132539.2-430957	543.6	13 25 39.2	–43 09 57.3	38	24.9	6.2	1.15×10^{37}		
255	CXOU J132615.9-425846	548.4	13 26 15.9	–42 58 46.8	530	392.4	23	4.70×10^{37}		
256	CXOU J132546.4-430937	549.4	13 25 46.5	–43 09 38.0	119	102.7	10.9	4.67×10^{37}		
257	CXOU J132450.4-430722	553.0	13 24 50.5	–43 07 22.9	271	151.4	16.5	2.17×10^{37}		
258	CXOU J132557.4-425342	553.8	13 25 57.5	–42 53 42.2	282	136.4	16.8	1.52×10^{37}	FS	GF Blue 1
259	CXOU J132525.9-425152	556.4	13 25 26.0	–42 51 52.7	160	96.2	12.7	1.44×10^{37}		
260	CXOU J132549.3-425241	560.6	13 25 49.3	–42 52 41.4	897	757.4	30	1.55×10^{38}		
261	CXOU J132503.1-430924	563.6	13 25 03.1	–43 09 24.3	163	85.2	12.8	1.28×10^{37}		
262	CXOU J132510.9-425214	564.4	13 25 11.0	–42 52 14.8	109	56.3	10.4	9.01×10^{36}		
263	CXOU J132534.0-431030	565.8	13 25 34.0	–43 10 30.2	46	34.5	6.8	1.61×10^{37}		
264	CXOU J132613.0-425632	569.9	13 26 13.1	–42 56 32.9	142	68.8	11.9	7.77×10^{36}		
265	CXOU J132620.4-425947	585.6	13 26 20.5	–42 59 47.2	142	78.6	11.9	1.94×10^{37}		
266	CXOU J132619.7-430318	586.0	13 26 19.7	–43 03 18.8	75	52.7	8.7	2.60×10^{37}		
267	CXOU J132454.4-425326	588.5	13 24 54.4	–42 53 26.8	65	35.2	8.1	7.91×10^{36}		
268	CXOU J132541.7-425137	592.0	13 25 41.7	–42 51 37.3	24	18	4.9	8.28×10^{36}		
269	CXOU J132541.9-431041	593.6	13 25 41.9	–43 10 41.4	642	610.1	25.3	2.86×10^{38}	GC	pff-gc-188
270	CXOU J132544.2-425141	595.8	13 25 44.3	–42 51 41.7	18	12.9	4.2	5.96×10^{36}		
271	CXOU J132548.4-425156	597.4	13 25 48.5	–42 51 56.9	25	20.8	5	9.54×10^{36}		
272	CXOU J132531.0-431105	597.7	13 25 31.0	–43 11 05.3	152	139.1	12.3	7.25×10^{37}	GAL	pff-qso-6

(1) – The sequence number; (2) – CXO source name, according to the *CHANDRA*-discovered source naming convention; (3) – distance from the center in arcsec; (4), (5) – right ascension and declination, J2000; (6) – total number of counts in the `wavdetect` source cell, source+background; (7) – number of source counts after background subtraction (8) – statistical error on the number of source counts after background subtraction; (9) – X-ray luminosity, 0.5−8 keV, assuming 3.5 kpc distance; (10) – source type: GC – confirmed globular cluster, FS – foreground star, GAL – background galaxy, H_α – H_α emmitter; (11) – precise identification and reference: pff – Peng et al. (2004), Tables 5 and 9; mrfa – Minniti et al. (2003), Tables 1 and 3; whh – Woodley et al. (2005) Tables 1 and 2 ; GF – Graham & Fasset (2002) Table 1; Kraft – Kraft et al. (2001) Sect. 5.1; HD – Roeser et al. (1991).

Comments: Source #121 was designated a globular cluster by Minniti et al. (2003), but according to Woodley et al. (2005) it is a background galaxy; Minniti et al. (2003) claim to have removed sources with H_α-emission from their list of globular clusters. However two sources (#54 and #108 in our source list) are both listed as H_α-emitters and globular clusters in their tables. We assume that they are H_α sources and designate them accordingly. Sources #146, #148 and #197 are included in the list of globular clusters of Minniti et al. (2003), although no colours are available. They are marked as globular cluster in the table.